Readout of fast signals with a multichannel sampling module

Bachelor Thesis
in the Department of Physics
at the Westfälische Wilhelms-Universität Münster

submitted by
Felix Ehring

Westfälische Wilhelms-Universität Münster
Institute of Nuclear Physics
AG Andronic
September 2022

Erstgutachter: Prof. Dr. Anton Andronic
Zweitgutachter: Prof. Dr. Christian Klein-Bösing

Contents

Chapter 1

Introduction

In today's world, the life we know is only possible because of the developments in the fields of science. It is striking that we are surrounded by technology and machines everywhere. They give us the opportunity to live a comfortable and long life.
Many of the modern technologies have been created due to research in laboratories. Especially in physics, time measurements are indispensable. They are often the limiting factor for the accuracy of the experiment and therefore improving the time resolution affects a wide range of developments.
In nuclear physics, an easy operation through USB readout, suitable for detector readout at small and large scales is needed. Therefore, the SAMPIC waveform digitizer, a high-precision and low-cost sampling module for particle and radiation detectors can be used. It attempts to increase time resolution to a new level of accuracy.

One project in which SAMPIC is already being used is, for example, the TOTEM experiment at the LHC. The word TOTEM is an acronym for Total Elastic and Diffractive Cross Section Measurement and is the name of a project at the world's largest particle accelerator LHC at CERN. It aims to determine the mass of the proton with unprecedented accuracy.
To do so, accelerated protons collide head-on at the LHC. The TOTEM is the only experiment at CERN being able to examine the protons, emerging at small angles from the collision, known as the forward direction. Therefore, detectors are distributed about 500 meters around the CMS interaction point. These detectors include four particle telescopes and 26 Roman Pot detectors. The telescopes are for examining the emerging particles and the Roman Pot detectors are for examining the scattered protons [CER22].
In 2017 an upgrade for the TOTEM was planned. It included the installation of timing detectors in the vertical Roman Pots. The read-out of these detectors was performed

with the SAMPIC chip because it is fast enough to sustain the information at the rate of the TOTEM. In addition, the cost per channel is comparable to that of a commercial time-to-digital converter, while no information is lost due to a discriminator in the structure. This is why the SAMPIC was preferred to the usual setup with a TDC and discriminator.
With the additional time detectors and the readout with the SAMPIC, an even higher accuracy should be achieved [Min+17].

Besides the use for scientific research, the readout of particles and radiation with detectors is also used in medical imaging. Thus, the read-out with SAMPIC could enable great progress in this area as well.
For around 50 years PET is no longer indispensable for medical imaging. In combination with X-ray computed tomography and magnetic resonance imaging, it already enables highly accurate imaging in cancer diagnosis. PET uses the arrival time of two photons created by the annihilation of a positron from the contrast agent with an electron from the tissue. The two photons are created simultaneously and travel in exactly opposite directions due to the conservation of momentum. A set of detectors is placed around the examined body part. Two detectors then capture the photons and can recreate their point of origin through arrival time and the addressed detectors. Since the creation of the photon pairs takes place simultaneously at different places, it can happen that two photons hit the detectors in quick succession, even if they come from different events. The detectors can only filter out these fake coincidences by their time of arrival. Therefore, this number can be decreased by increasing the resolution of the detector. With a resolution of 10 picoseconds for the FWHM, as targeted by SAMPIC, a 3D volume representation of the activity distribution would be possible in real-time [Lec+20].
Current PET scanners only have a resolution of 214 ps. With the considered increase way smaller tumours could be detected, that would have been missed before. Besides small tumours, the reduction of false coincidences would affect the screening of lung cancer. With current resolutions, it has a false positive rate of 96%, which would be decreased. In addition, less contrast agent would be needed and a clearer image could be contained for a longer time. This would also allow a larger area of the body to be studied with the same number of detectors. A whole body-sized measurement could even be possible [Lec+20].

Overall, the selection of fast signals thus represents a great opportunity to improve a wide variety of projects in science. For this reason, the following bachelor thesis deals with exactly this readout of fast signals with a multichannel sampling module, as it is SAMPIC. In order to be able to evaluate the first readout with the SAMPIC, known signals are to be investigated. These are the measurement of cosmic rays with scintillation detectors. The SAMPIC and the digital readout then should allow for examining the distribution of the amplitude and the full width at half maximum of the signals. In order to take advantage of the multiple channels and the high resolution of the SAMPIC, coincidences were subsequently measured using the detectors already investigated. This measurement then allowed the examination of the resolution of the given detector setup. A successful readout of known signals would allow the investigation of unknown signals with the SAMPIC.

Chapter 2

Theoretical Background

2.1 Cosmic Radiation

To measure coincidences with the given detectors, high-energy radiation is required, which can pass through the first detector and still have sufficient energy to be detected in the second detector. The easiest way to achieve this is to use the cosmic particle radiation that continuously hit the earth.
Due to the comparatively short distance, most of the particles hitting the earth come from our sun. They are generated during events such as solar winds or solar flares and consist mainly of protons and alpha particles. When these particles reach the earth's atmosphere, they interact with the atoms and form a particle shower. In such a shower pions are produced, which decay into muons, muon neutrinos and gamma quants after the relations:

$$\begin{aligned}\pi^+ &= \mu^+ + \nu_\mu \\ \pi^- &= \mu^- + \bar{\nu}_\mu \\ \pi^0 &= \gamma + \gamma\end{aligned}$$

In general, the resulting muon travels in the same direction as the pion did. The muons are heavier than an electron but much lighter than all the matter particles and have the same negative elementary charge as an electron [Gru18]. The only reason why muons reach the earth's surface within their half-life is their high energy based on their high speed, which is almost equal to the speed of light. They have energy in the magnitude of a few TeV, which is why they can travel almost a kilometre in water and about 2.4 km in ice. Therefore, they can reach the earth's surface and can be detected in the first and the second scintillation detector, and even through walls [KW16].

2.2 Interaction of Particles and Radiation with Matter

2.2.1 Interaction of Particles with Matter

To be able to detect any kind of particle or radiation, their interaction with matter has to be understood. The first important interaction is the energy loss of charged particles due to ionization or stimulation of electrons in the atomic shell. It can occur after a particle collides elastically with such an electron. Besides the shell electrons, a particle can also collide with the core. In this case, a distinction is made between an elastic impact, in which the core receives only a small and negligible recoil, and an inelastic impact, in which the core may even be excited. After an excitation, it returns to the ground state and emits a photon or thermal energy [Dem17].

In total, the energy loss due to ionization for all the charged particles heavier than electrons and positrons can be described with the Bethe-Bloch-Formula in Equation 2.1 with the charge number z and velocity β of the projectile particle, the atomic number Z and the mass number A of the medium, a constant factor K, the mean energy for ionization of the medium I and the maximum energy transfer to a shell electron T_{max}.

$$-\left(\frac{dE}{dx}\right) = K\frac{Z}{A}\rho\frac{z^2}{\beta^2}\cdot\left[\frac{1}{2}\ln\left(\frac{2m_e c^2\beta^2\gamma^2 T_{\mathrm{max}}}{I^2}\right) - \beta^2 - \frac{\delta(\beta\gamma)}{2} - \frac{C(\beta\gamma, I)}{Z}\right] \tag{2.1}$$

In addition, two correction terms are added to this formula. The first one includes the density correction δ for high energies and the second one is the so-called shell correction $\frac{C}{Z}$ for small energies [KW16].

When light particles such as an electron or a positron are the incoming particles, deflection occurs due to the coulomb field of the atomic core. The resulting loss of energy of the electrons leads to the so-called bremsstrahlung. The electrons are decelerated and emit this radiation, which is proportional to the square of the deceleration [Dem17].

For ionization and bremsstrahlung, the Equation 2.2 and the Equation 2.3 for the energy loss per travel length with the energy of the particle E, the mass of the particle M and the nuclear charge Z of the medium are valid.

$$\text{Ionization :} \qquad -\frac{dE}{dx} \propto Z\cdot\frac{\ln(E)}{M} \tag{2.2}$$

$$\text{Bremsstrahlung :} \qquad -\frac{dE}{dx} \propto Z^2\cdot\frac{E}{M^2} \tag{2.3}$$

This progression is shown in Figure 2.1. For small energies, the energy loss due to ionization is the dominant process. With increasing the energy the energy loss of the radiation due to the deceleration becomes dominant. For a specific critical energy E_c the energy loss is identical and the two curves intersect. This energy is an important parameter for some physical phenomena like the generation of an electric magnetic shower [KW16].
Because of their proportionality to $\frac{1}{M}$ and $\frac{1}{M^2}$ respectively, the influence of the two mechanisms for energy loss decrease for heavier particles like muons or pions. However, cosmic muons or muons in a particle accelerator can have energies in the range of several TeV, which is high enough for bremsstrahlung and ionization to be dominant nevertheless [KW16].

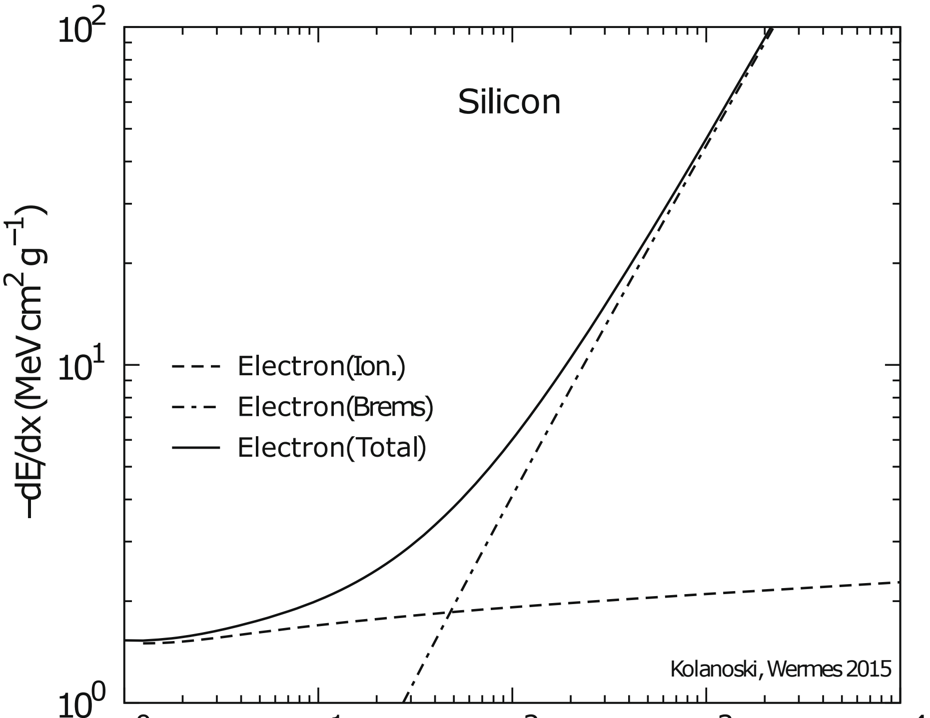

Figure 2.1: The energy loss due to ionization and bremsstrahlung for electrons as a function of time. The sketch is from [KW16], with altered labelling.

2.2.2 Interaction of Radiation with Matter

When particles interact with matter they often emit a photon, which can interact with the matter itself. This interaction of radiation and photons with matter is often distinguished where the photon meets the atom. When the photon is deflected at an electron that is far from the nucleus, the Compton effect occurs. Such an electron is described as quasi-free if the binding energy is essentially smaller than the energy of the photon. In that case, the deflection can be described as elastic and after the collision both, the photon and the electron, travel in different directions away from the atom. The received kinetic energy corresponds to the amount of energy the photon loses through this hit. A small amount of energy is required to overcome the binding energy of the electron, but since this is described as nearly free, it is much less than the kinetic energy and can be neglected. The kinetic energy results from the relation

$$T = E_\gamma - E'_\gamma \tag{2.4}$$

with the photon energy E_γ before and E'_γ after the collision. The exact amount of energy the photon loses depends on how head-on it hits the electron. The maximum energy transfer occurs when the photon hits the electron directly and is backscattered by 180° [KW16].

The photon can not only be scattered but also absorbed by the atom, which mainly happens for photons with an energy above 1 keV. This process is called the photoelectric effect. The atom receives a recoil during the collision, which is important for the conservation of momentum. Due to the high mass of the atom, this recoil is again negligible. Moreover, the atom not only absorbs the momentum of the photon but is also ionized by the interaction. The ionized electron has kinetic energy, which resembles the difference between the energy of the photon and the binding energy of the electron. Therefore, the relation

$$T = E_\gamma - E_\mathrm{b}, \tag{2.5}$$

with the complete energy of the photon E_γ and the binding energy E_b, is valid. For the photoelectric effect to occur at all, the photon energy must be higher than the binding energy. However, the cross-section of the photoelectric effect decreases rapidly with increasing photon energy. If the photonic energy is constant and the atomic number increases, the cross-section increases too. When both the energy and the nuclear charge number are constant, absorption by the most bound electron with binding energy below the photon energy is most likely. Therefore, jumps can be observed while increasing the photon energy every time it reaches the binding energy of a new shell. These jumps are called absorption edges [KW16].

If the photon is in a coulomb field and has energy above

$$E_\gamma \approx 2 \cdot m_e \cdot c^2 \tag{2.6}$$

with the mass of an electron m_e, pair production can occur. As the name already indicates, it describes the production of an electron-positron pair. Because of their opposing charge, the conservation of energy is given. To additionally achieve conservation of momentum, the atomic core once again has to take the recoil of the collision. Thus, pair production mainly occurs in the coulomb field of the core. Similar to the photoelectric effect the energy transfer via recoil can be neglected for Equation 2.6 [KW16].

The three different processes are each dominant for a certain photon energy E_γ and the nuclear number Z. For the cross-section of the Compton effect, the relation

$$\sigma_c \propto \frac{Z}{E_\gamma} \tag{2.7}$$

applies for $E_\gamma \geq m_e c^2$. The cross-section of the photoelectric effect is even more dependent on the given parameters with

$$\sigma_{\text{ph}} \propto \frac{Z^5}{E_\gamma^{\frac{7}{2}}} \tag{2.8}$$

for $E_\gamma > E_\text{b}(k)$ with the binding energy of the k-shell. When the energy increases to $E_\gamma \gg E_\text{b}(k)$ the relation changes to

$$\sigma_{\text{ph}} \propto \frac{Z^5}{E_\gamma}. \tag{2.9}$$

In case of the cross-section of the pair production, the proportionality

$$\sigma_p \propto Z^2 \cdot \ln(E_\gamma) \tag{2.10}$$

is valid. The progression of the three cross-sections for a lead absorber with $Z = 82$ can be seen in Figure 2.2. It displays the curves in which the cross-sections for the photoelectric and the Compton effect, and for the Compton effect and pair production are equal. In addition, Figure 2.3 shows the curve representing the values where the photoelectric effect and the Compton effect, and the Compton effect and the pair production have the same cross-section depending on the two parameters. For a small nuclear number of the absorber, the Compton effect is dominating for almost every energy from 0.01 MeV up to 100 MeV. For higher values of Z this range gets smaller and the photoelectric effect and pair production are dominating [Dem17].

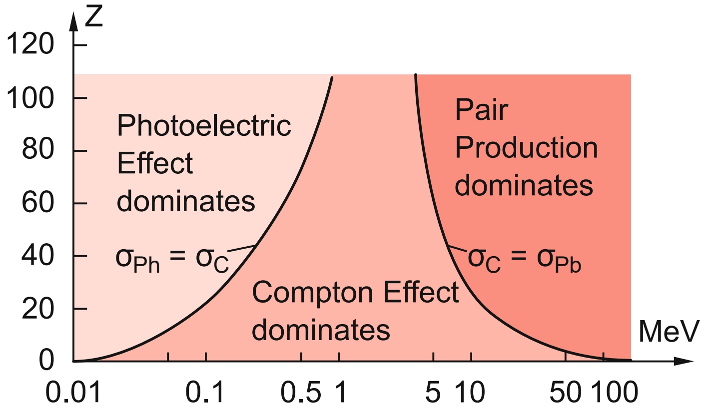

Figure 2.2: The areas in which the Compton effect, the photoelectric effect and pair production are dominant, depending on the nuclear number of the absorber and the energy of the photons. The figure is from [Dem17] with altered labelling.

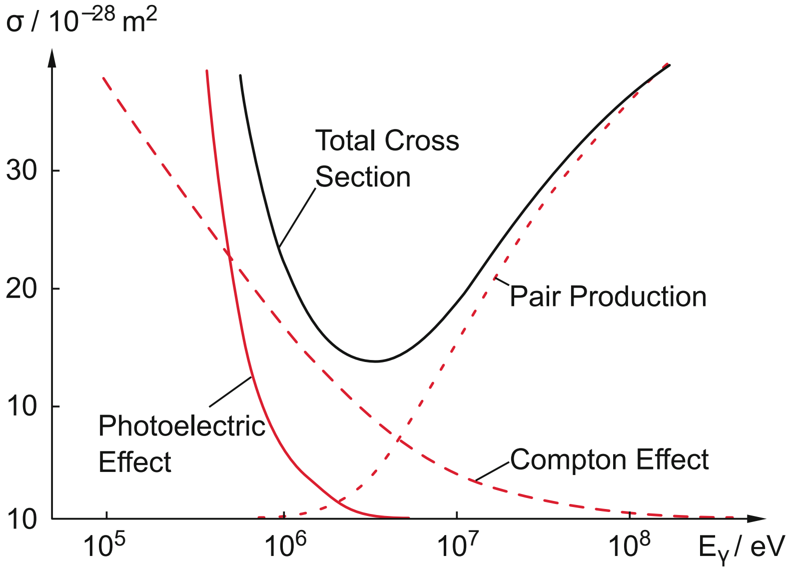

Figure 2.3: The different cross-sections for the photoelectric effect, the Compton effect, and pair production along with a resulting total cross-section for a lead absorber as a function of photon energy. It is from [Dem17] with altered labelling.

2.3 Scintillator

To detect radiation or particles a scintillator is a commonly used detector type. The word scintillator derives from the Latin word *scintillare*, which means to sparkle. A scintillator produces luminescence by absorbing ionizing radiation or particles. In case of charged particles, it either comes from ionization following recombination in the scintillating material or due to molecular excitation and the subsequent transition to the ground state. Photons, on the other hand, produce luminescence indirectly via electrons generated by interactions with the scintillator. These electrons are again the reason for ionization of the atoms in the material [KW16].

The tasks of a scintillator are energy measurement of the above-mentioned radiation and particles and generation of fast electrical signals, which can be used to measure the time of flight or used as a fast trigger. Therefore, the scintillator needs to have a short duration for the creation of luminescence to enable faster signal generation. Another important property is that the number of photons of a given wavelength per energy of the incident radiation is proportional to the emitted energy. Only under this condition, it is possible to draw conclusions about the incoming energy on the basis of the light measurement. In order to operate the scintillator optimally, it must additionally be transparent to the wavelength of the emitted light and have the highest possible light collection efficiency [KW16].

2.3.1 Organic Scintillators

When describing the mechanism in detail, it is necessary to distinguish between organic and inorganic scintillators. The first scintillator used was a plastic scintillator, which is organic. These types of scintillators, as the name implies, are based on carbon compounds. When carbon goes into a compound with another carbon atom its orbitals hybridize. This means, that some of the three $2p$-orbitals mix with the $2s$-orbital. When all three $2p$-orbitals mix, the atom is sp^3 hybridized. If only two $2p$-orbitals are in the mixed orbital configuration, it is sp^2 hybridized. If it is just one $2p$-orbital together with the $2s$-orbital, the hybridization is called sp-hybridization. In the second last hybridizations, one or two $2p$-orbitals, respectively, do not change compared to their unbound state. The electrons in these orbitals, called π-electrons, provide luminescence because they are less strongly bound than the σ-electrons in the hybridized orbitals. Therefore, the π-electrons can get excited easier than the σ-electrons. In addition to the main energy levels, there are various sublevels, also called vibrational states. While the transition from one such sublevel to another or the next main state is often radiationless, the transition from the main states to the ground state is based on the emission of photons. The mechanism is called prompt fluorescence and takes place in a magnitude of some nanoseconds. It is the main process in a pure material.

A plastic scintillator like the one used in this setup is based on a liquid scintillation compound. Polymerisation can turn them into solid scintillators of any shape. Frequently used materials are polystyrene, polyvinyl toluene or polymethylacrylate [KW16].

2.3.2 Inorganic Scintillators

The second scintillator used was based on a barium fluoride crystal and was thus inorganic. The luminescence of inorganic scintillators is based on the lattice structure of the crystals. To explain this mechanism the band structure of a crystal needs to be understood. Two bands, in particular, are the most important for the description. The conduction band, the occupied band with the highest energy, and the valence band, the band directly above it. In the conduction band, the electrons can move almost freely, while in the valence band they have a fixed place because it is fully occupied. In the case of a metal, both bands are in contact and the electrons can move to the conduction band easily. That is why metal is conductive [KW16].

In a non-metal crystal, the two bands are divided by a band gap. This gap is about 4-12 eV for a scintillator. The stimulation of an electron from the valence band into the conduction band can create a hole in the valence band. This stimulation can occur again by ionizing radiation or matter. Due to the size of the band gap, the energy released by recombination after such a stimulation corresponds to a photon wavelength outside the visible range. Therefore, for a crystal to scintillate so-called luminescence centres are needed. They are in between the two bands and have an energy level smaller than the band gap. Instead of the electron returning to the valence band with one step of the size of the band gap, it goes from one luminescence centre to another. The energy released between each state corresponds to a photonic wavelength in the visible range, which allows the crystal to scintillate [KW16].

A sketch of such a band structure is depicted in Figure 2.4. If a transition is small enough, it can be radiation-free and for example thermal instead. The effect of a radiation-free transition can also occur between the luminescence centres although the energy is high enough for luminescence. Under these circumstances, one speaks of quenching. Some reasons for quenching are the formation of complexes within the material or a transfer of energy to a so-called quencher, which is a molecule that can store the spare energy [KW16].

Another process shown in Figure 2.4 is trapping. Caused by lattice defects a new energy level can be created, which can hold the electron for an indefinite time. When an electron is trapped, it either gets stimulated in the conduction band again or returns to the ground state without radiation. These traps allow the generation of radiation that is more energetic than the visible spectrum for example ultraviolet radiation [KW16]. Another effect, which can occur, is the generation of an exciton. When an electron gets stimulated it is possible that a hole gets attracted, because of their electric field, and the two recombine. The exciton, which is a quasiparticle, corresponds to an energy level just below the conduction band. Therefore, with a small amount of energy the electron can be stimulated into the conduction band. This exciton can move freely in the crystal until it decays [KW16].

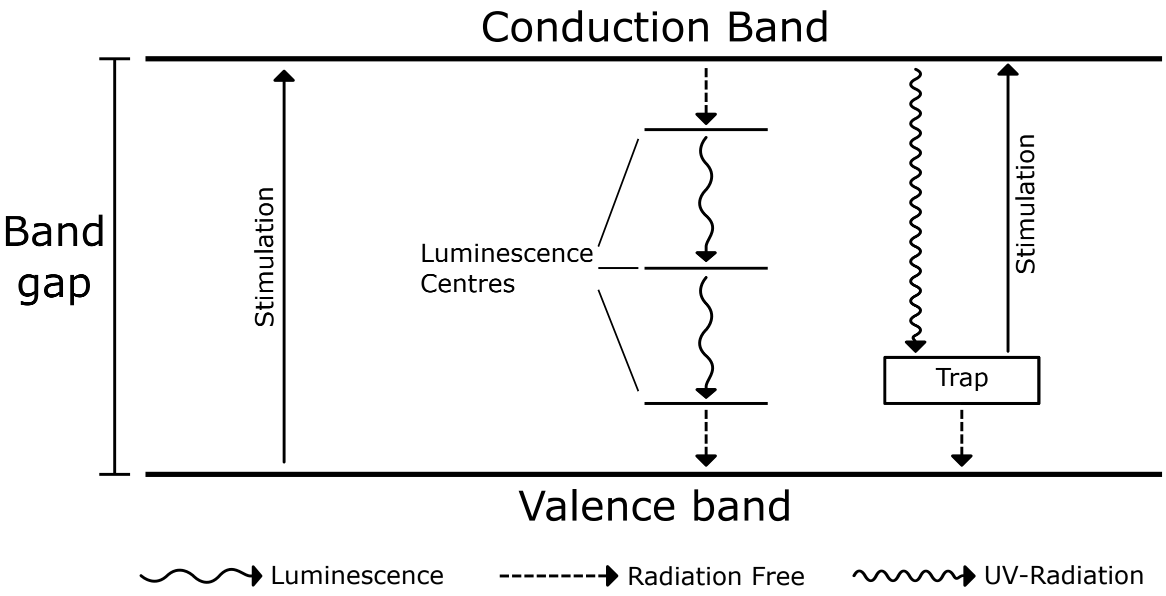

Figure 2.4: A sketch of an inorganic scintillator together with its conduction and valence band, the band gap, the luminescence centres and an example of a trap. The different types of transitions are indicated with different types of arrows.

Inorganic scintillators often have a rise and decay time of a magnitude of some hundred nanoseconds, which is larger than the rise and decay time of a few nanoseconds of organic or especially plastic scintillators. Even though the BaF_2 is one of the fastest inorganic scintillators and much closer to the values of plastic scintillators, it still has a longer rise and decay time. Plastic scintillators are the ones to use for time-critical processes or fast trigger mechanisms. In terms of luminous efficiency, an inorganic scintillator is also inferior to a plastic scintillator. The reason why inorganic scintillators nevertheless have many applications is due to their higher density. It allows them to examine high-energy particles or photons, because of their ability to completely absorb them at a lower depth. For these particles, the luminous efficiency and the downtime are less important than the opportunity to absorb the whole energy of the incoming radiation [KW16]. Regarding the measurement of cosmic muons, longer rise and decay times have a small impact, because less than 10 muons per second travel through the small entrance window of the detectors used. Therefore, both of the scintillators are fast enough for this kind of measurement.

2.4 Photomultiplier

A PMT, short for photomultiplier, is directly connected to the scintillator. For the most efficient connection, the refractive index between the PMT and the scintillator should be close together. This is usually ensured with a light guide. The Figure 2.5 shows a sketch of such a PMT. Photons generated in the scintillator pass through an entrance window onto the photocathode of the photomultiplier. Within the photocathode, the valence electrons are poorly bound and have a great profile for the conversion of photons into electrons. This conversion occurs through the photoelectric effect. The incoming photons have the energy to release an electron from the cathode material [KW16].

Theoretically, one could simply detect this electron directly with a measuring device. However, at the time of the invention of the photomultiplier, no measuring device was accurate enough to detect a deflection of a single electron. Even today, a direct measurement of such an event would be too error-prone and even hard to perform at all. Therefore, the signal has to be amplified which is done in the second part of the PMT [KW16].

After the electron is generated, it is accelerated towards the first dynode due to a potential difference. Through this acceleration, the electron gains enough kinetic energy to liberate up to 4 electrons from the dynode material. The following dynode has an even less negative voltage applied than the current one. This causes the generated electrons to be accelerated towards the second dynode, where in turn the same effect occurs. It is repeated for all of the dynodes until the electrons reach the anode, which voltage is on ground level. In total, this setup leads to an amplification in the magnitude of 10^5 up to 10^7. The resulting peak at the final anode is easy to read out and contains all the information about the energy of the incoming photon [KW16].

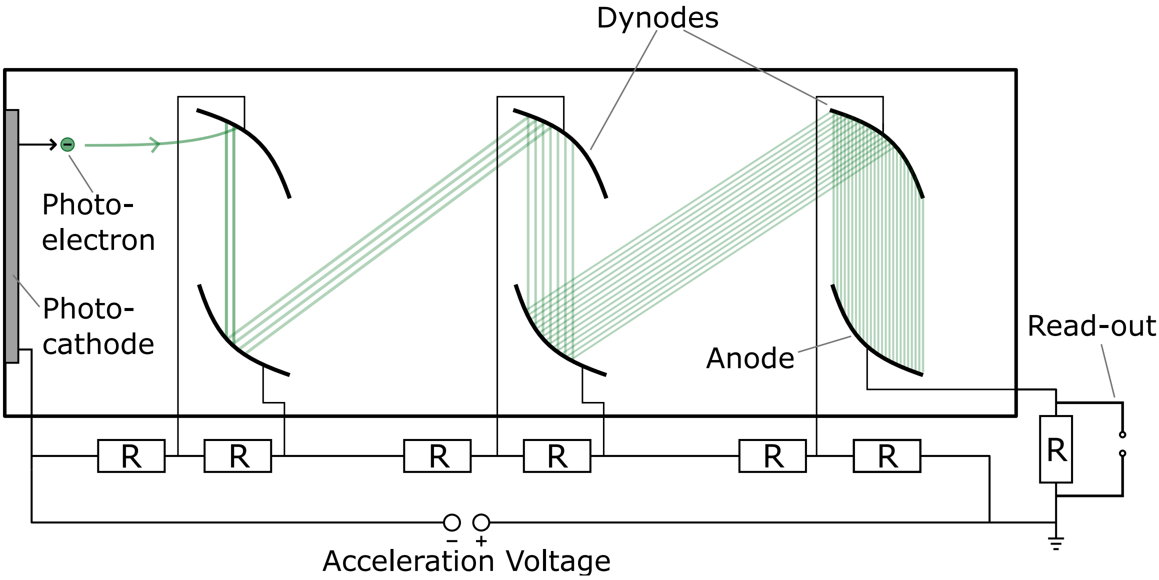

Figure 2.5: A sketch of a photomultiplier with its photocathode, dynodes, end anode, power supply and readout section. The different potentials at the dynodes are generated with resistors, across which a certain part of the voltage is dropped.

Chapter 3

SAMPIC Waveform Digitizer

The SAMPIC waveform digitizer was developed by CEA/IRFU/SEDI, Saclay and CNRS/LAL/SERDI, Orsay to perform precise time measurements in the order of picoseconds. Hence the name SAMPIC, which is composed of the words SAMpler for PICosecond time. Time measurements are needed in almost every field of science. For example at the Large Hadron Collider at CERN the time of arrival of two particles can be used to calculate their vertex. This method allows verifying if the particles come from the main interaction or from other sources or the background. With a time precision of 10 ps, which is typical and calculated with the root mean square method (short RMS), a precision of ±2 mm can be reached. The time resolution of the SAMPIC chip should be about 5 ps RMS, which would result in an even more precise calculation of the vertex and reduction of background events [Bre⁺16].

3.1 The SAMPIC Chip

Systems for time measurement are usually based on Time to Digital Converters, short TDC. They work with a counter to achieve coarse timing and a Delay Locked Loop, short DLL, to do a finer interpolation. That is why the precision of the timing relies on the steps of the DLL. This technique only allows a resolution of around 20 ps RMS. If the incoming signal is an analogue pulse, a fast discriminator is needed to create the digital signal the TDC needs. However, this discriminator leads to increased jitter and limits timing precision [Bre⁺16].

Therefore, this approach is not suitable for the SAMPIC chip and the targeted time resolution. The SAMPIC, on the contrary, is based on a so-called waveform-based TDC, or WTDC. This approach uses a fast digitizer connected in parallel with the delay line and based on an analogue memory that allows capturing the time-relevant part of the analogue input, e.g. the time stamp for reaching a certain threshold. Figure 3.1 shows a sketch of the functionality of one channel of the SAMPIC chip. By applying interpolation through the digital data a time resolution of a few picoseconds can be achieved. A picture of the SAMPIC module can be seen in Figure 3.2 [Bre+16].

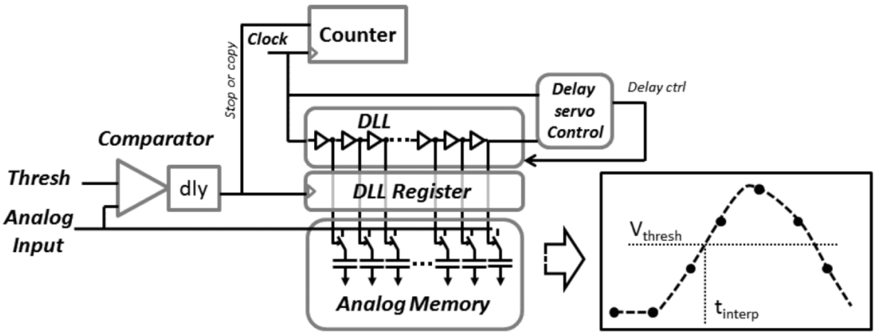

Figure 3.1: A sketch of one channel of the SAMPIC [Bre+16].

Figure 3.2: A picture of the SAMPIC module.

3.2 Software

3.2.1 The Online Control Software

The SAMPIC WTDC can be controlled with software based on LabWindows libraries. It allows real-time measurements and to set the sampling parameters like sampling frequency, baseline or ADC range, trigger parameters and acquisition parameters. To increase the time resolution from 15 ps RMS up to less than 5 ps RMS two types of calibrations are implemented in the software. One is used to improve the linearity of the analogue-to-digital converter, and the other to correct the sampling period in the analogue memory if it is not uniform. Both calibrations have to be done for every set of acquisition parameters [Bre+16].

3.2.2 The Offline Software

To examine the time precision of the SAMPIC chip an offline software based on C++ in the ROOT framework can be used. Two different reconstruction algorithms are implemented in this software.

The first is the CFD algorithm, which stands for Constant Fraction Discriminator. Here the threshold is defined by a given fraction of the signal's amplitude. When the signal reaches this specified proportion, the arrival time is measured. This definition of the threshold leads to a result, which is independent of the signal's amplitude and suppresses the time walk effect. Besides the normal CFD algorithm, a refined version is also implemented in the software. This version measures the arrival time for multiple different fractions and then calculates the average. When more than two points lay on the rising edge, the refined version can increase the resolution of this method [Bre+16].

The second implemented algorithm is the cross-correlation, short CC. This algorithm computes a cross-correlation between the acquired signal and a template from a set of acquisitions with high statistics. This template needs to contain an independent measurement under similar conditions as the signal. By delaying one of the parts in steps of 1 ps, the maximum of the correlation can be found [Bre+16].

In summary, the CC is more expensive to operate. A template suitable for the measurement, which will be taken, needs to be generated and the computation time is about 100 times higher than for the CFD. However, the CFD relies entirely on a few points on the rising edge and is therefore much more prone to uncertainty and errors [Bre+16].

3.3 Tests for Resolution

3.3.1 Tests with Signal Generator

The first test was performed with signals from a signal generator. The signals were divided and sent to two different cables with different lengths to achieve a delay between them. The signal generator had a rise time below 1 ns and the sampling speed of the SAMPIC was set to 6.4 GS/s. For the analysis, 10000 events were processed with the three algorithms. The threshold for the CFD was set to $R = 0.5$ and the refined CFD averaged between values between $R = 0.3$ and $R = 0.7$ in steps of $R = 0.05$. The results are indicated in Figure 3.3. It shows the RMS of the time difference in nanoseconds depending on the signal amplitude for the three algorithms and a theoretical course for the CFD with a value for the fraction of $R = 0.5$. The theoretical predictions were calculated with the RMS noise in each channel. Figure 3.3 shows, that the refined CFD, labelled as R average, provides slightly better results than the classic CFD for every amplitude and is closer to the theoretical value. For low amplitudes around 0.4 V, the signal over noise ratio is very low. Therefore, the cross-correlation provides a RMS of the time difference, which is up to 50% smaller. While the two CFD algorithms produce a time difference of around 27 ps RMS the CC is about 14 ps RMS. With an increase in amplitude, the time difference decreases rapidly. For an amplitude around 0.1 V all the algorithms provide a value below 8 ps RMS and are closer to each other.

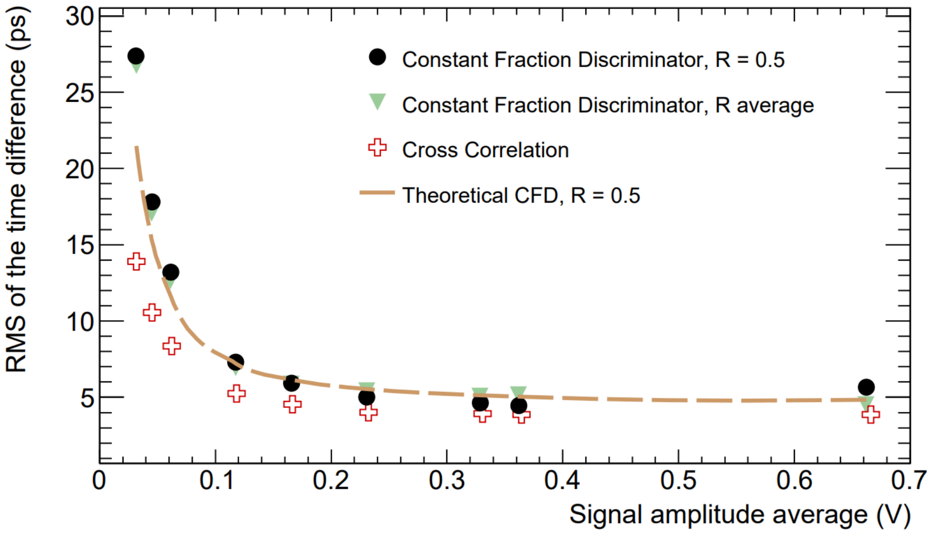

Figure 3.3: The RMS of the time difference of two signals from a signal generator in relation to the signal amplitude. The time difference was calculated with a CFD, a refined CFD and a CC algorithm. In addition, the figure includes the curve for a theoretical CFD [Bre^{+}16].

For amplitudes above 0.1 V the increase of the time difference is less fast and near constant for amplitudes above 0.6 V. There, the CC provides a time difference of around 4 ps RMS and is about 1 ps RMS smaller than the refined CFD and about 2 ps smaller than the classic CFD. In conclusion, the SAMPIC reaches the goal of a resolution of 5 ps RMS with these ideal signals and as expected, the cross-correlation provides the best results [Bre+16].

3.3.2 Tests with Real Signals

To test the time resolution of two channels of the SAMPIC chip with real signals, ultra-fast silicon detectors, short UFSDs, were used. The signal source was a pulsed infrared laser. Its beam was split and then sent to two UFSDs with a jitter below 3 ps RMS between the two laser pulses. Afterwards, the signals each go through an amplifier and then into two different channels of the SAMPIC. The exact setup can be seen in [Bre+16]. Figure 3.4 shows the results for 10000 events. It again displays the RMS of the time difference in nanoseconds depending on the signal amplitude for each algorithm and the theoretical course, which was calculated with the RMS noise observed in the data. For small amplitudes around 0.1 V the RMS is below 110 ps for all the algorithms. The refined CFD provides an improvement of up to 20 ps RMS compared to the classic CFD and the cross-correlation is even up to 5 ps RMS better

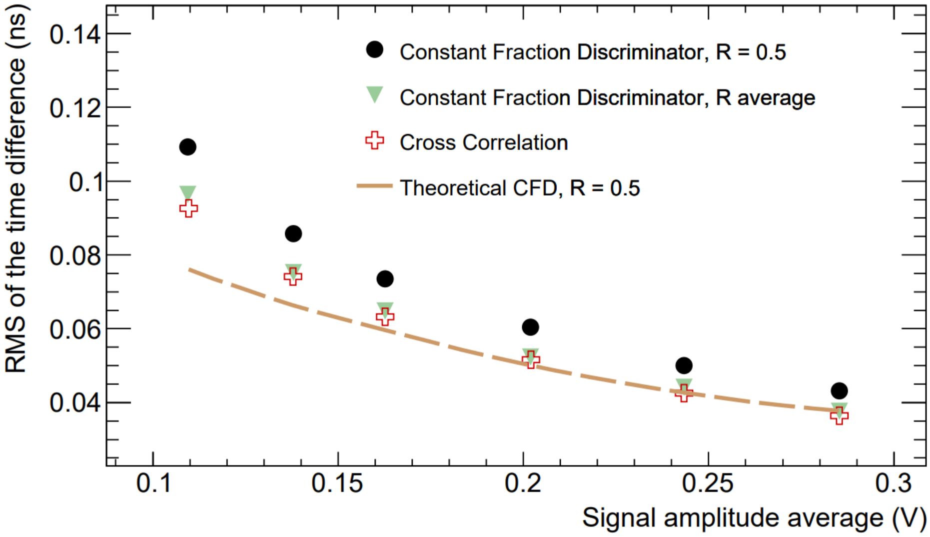

Figure 3.4: The RMS of the time difference of two real signals in relation to the signal amplitude. The time difference was calculated with a CFD, a refined CFD and a CC algorithm. In addition, the figure includes the curve for a theoretical CFD [Bre+16].

than the refined CFD [Bre$^+$16].

As the amplitude increases, the RMS value of the time difference decreases, because the signal-to-noise ratio increases. The decrease of the time difference is less rapid than for the signal generator and it does not stop in the given range of amplitude. Not only do the values of the three algorithms decrease, but they are also closer to each other and closer to the theoretical value for higher amplitudes. The fact that the refined CFD is closer to the classical CFD can be explained by a shorter ride time and fewer points taken for the refined CDF. For an amplitude of about 0.29 V all algorithms give a time difference around 40 ps RMS, where the CC is still better than the two CFDs. Here, however, the refined CFD is much closer to the cross-correlation and the theoretical value [Bre$^+$16].

A further test on the resolution of a single channel shows that the resolution for real signals is limited by the detector and the amplification chain and not by the SAMPIC chip. It is also noted that the performance does not decrease significantly whether the sampling frequency is 6.4 GS/s or 3.2 GS/s [Bre$^+$16].

Chapter 4

Methods, Results and Discussion

4.1 Methods

4.1.1 Experimental Setup

In order to perform the measurements, a high voltage power supply from CAEN for the photomultiplier in the detector together with the detector itself, the SAMPIC module connected to a computer and the online software for controlling the SAMPIC were needed. Two different detectors were used, which are shown in the appendix in Figure A.1 and Figure A.2. The first one was based on a plastic scintillator and the second one was based on a barium fluoride scintillator. The detectors got connected to the power supply over an HV cable and to the SAMPIC module with a LEMO cable. The SAMPIC was connected to the computer over an USB-A cable.

The first step was to find the right supply voltage for each detector. It had to be high enough to detect the cosmic radiation, but as low as possible to reduce noise. For this determination, the detectors were connected to an oscilloscope. This allowed examining the signals, before using the readout of the SAMPIC module. The first detector with the plastic scintillator needed a voltage of 1300 V and for the second detector with the barium fluoride scintillator an applied voltage of 1000 V was chosen. For both detectors the ramp up and down speeds were $50\,\frac{\mathrm{V}}{\mathrm{s}}$.
One important factor was the negative polarisation of the power supply. Otherwise, the PMT is not able to push the electrons to the different dynodes and there is no electron current to measure.
Additionally, both detectors were insufficiently light insulated or had a source of background noise too close to them. This problem was observed on the oscilloscope since almost one hundred smaller peaks per second were additionally displayed. The

magnitude frequency of muons detected on the small surface of the detector should be one or two particles per second. Therefore, an opaque cover was placed over each detector to prevent light from passing through while allowing cosmic rays still reach the detector. However, to completely prevent the additional signals, a suitable threshold had to be selected. This ensures that the signal-over-noise ratio is high enough for the analysis and the unwanted hits can be avoided. For the first detector a threshold of -20 mV and for the second detector a threshold of -40 mV were chosen. In both cases, the threshold was applied to the falling edge of the signal.
The sampling speed of the SAMPIC was set to $6.4\,\frac{\mathrm{GS}}{\mathrm{s}}$ for the first two measurements.

After examining the two individual detectors, a coincidence measurement was performed. Therefore, the entrance window of the plastic scintillator was placed on top of the barium fluoride scintillator. Nearly all particles going through the top detector should go through the detector below as well. The setup can be seen in Figure 4.1.

Not only the setup needed adjustments, the software settings too. The triggering mechanism had to be changed from single triggering of one detector to simultaneous triggering of both detectors when a particle passes through. For this reason, the thresholds stayed the same, but the trigger mechanism was changed from self-triggering

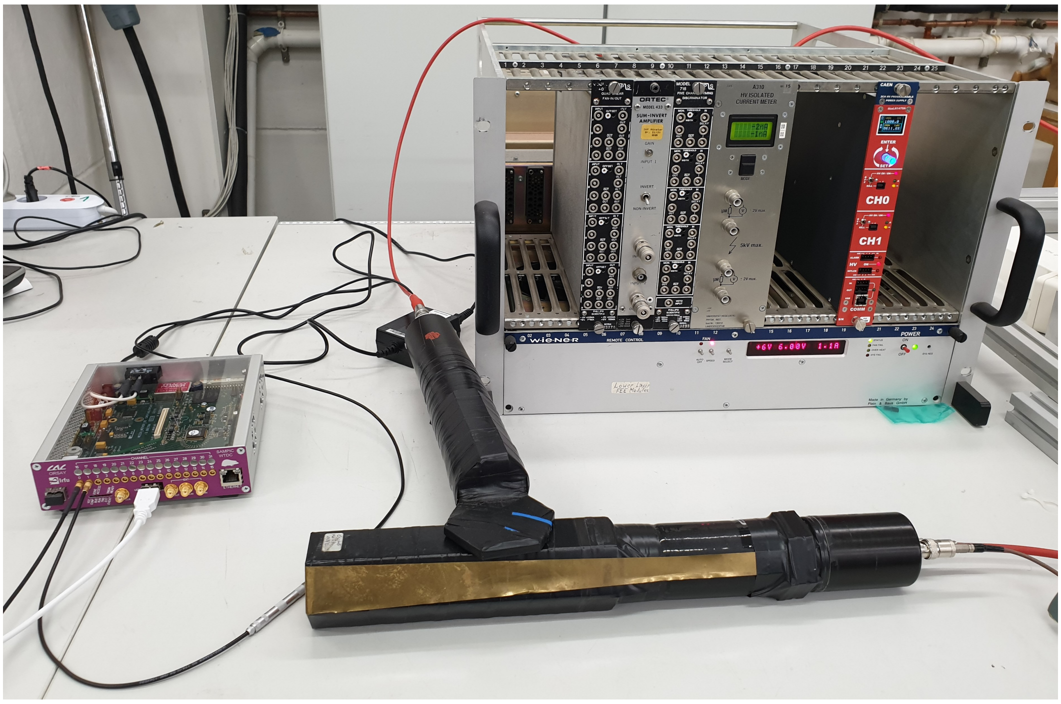

Figure 4.1: The setup for the coincidence measurements. The plastic scintillator on top of the BaF_2 scintillator can be seen, which are each connected to the power supply and the SAMPIC module.

to central triggering. The central trigger adjustments were set to trigger when both of the channels reach their thresholds at the same time. When this happens, both channels trigger and save the data. The settings in the software are displayed in Figure 4.2 (a). To increase the length of the time window, the sampling rate was reduced to 1.6 $\frac{\text{GS}}{\text{s}}$. The program stored 64 samples still, but as the time between samples increased, a larger part of the signal was measured. Additionally, it was also necessary to ensure that there was no delay between the trigger time and data acquisition, as this parameter is not set to zero nanoseconds by default. These settings can be seen in Figure 4.2 (b).

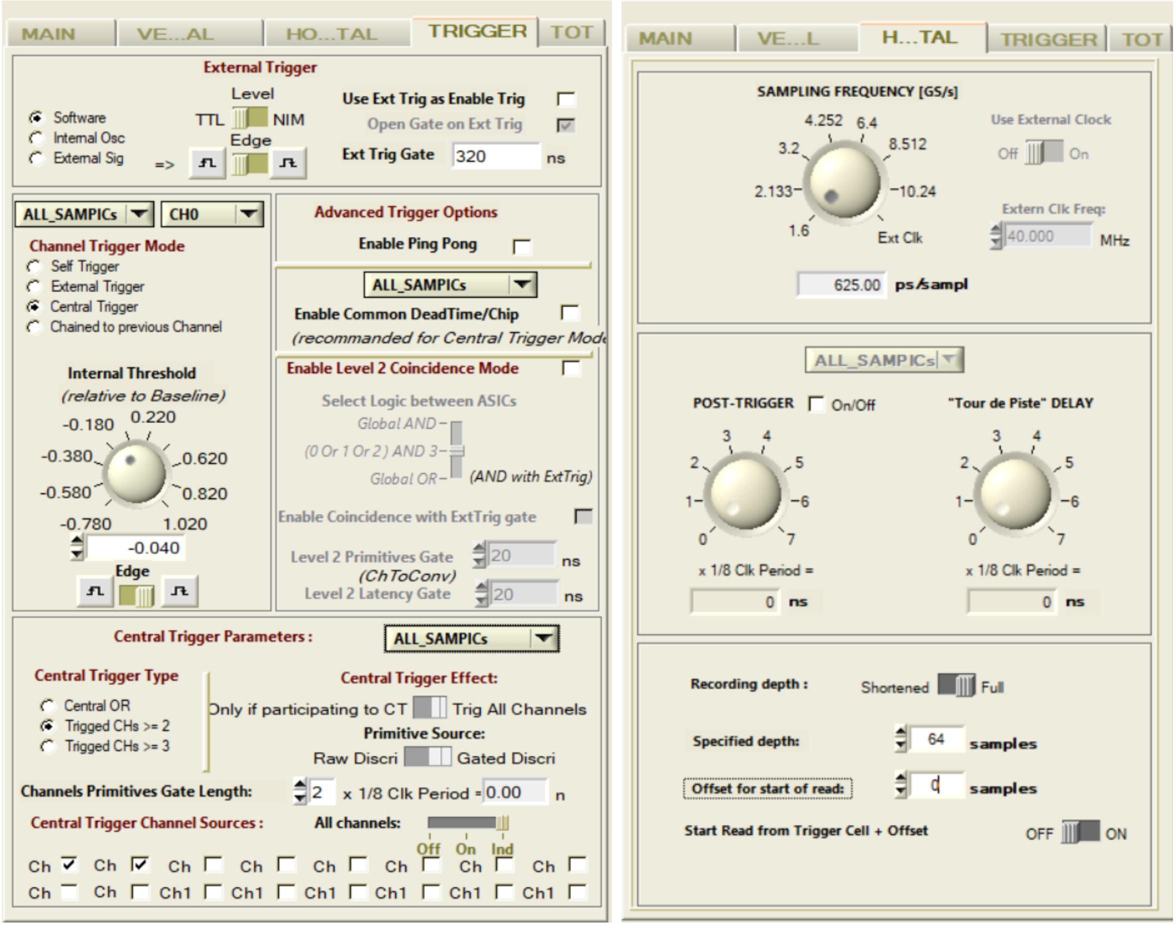

External Trigger

● Software
○ Internal Osc
○ External Sig

Use Ext Trig as Enable Trig ☐
Open Gate on Ext Trig ☑
Ext Trig Gate 320 ns

ALL_SAMPICs CH0

Channel Trigger Mode

○ Self Trigger
○ External Trigger
● Central Trigger
○ Chained to previous Channel

Internal Threshold (relative to Baseline) -0.040

Advanced Trigger Options

Enable Ping Pong ☐
ALL_SAMPICs
Enable Common DeadTime/Chip ☐
(recommanded for Central Trigger Mod

Enable Level 2 Coincidence Mode ☐
Select Logic between ASICs: Global AND / (0 Or 1 Or 2) AND 3 / Global OR (AND with ExtTrig)
Enable Coincidence with ExtTrig gate ☐
Level 2 Primitives Gate 20 ns
(ChToConv)
Level 2 Latency Gate 20 ns

Central Trigger Parameters: ALL_SAMPICs

Central Trigger Type:
○ Central OR
● Trigged CHs >= 2
○ Trigged CHs >= 3

Central Trigger Effect: Only if participating to CT / Trig All Channels
Primitive Source: Raw Discri / Gated Discri
Channels Primitives Gate Length: 2 x 1/8 Clk Period = 0.00 n
Central Trigger Channel Sources: All channels:

Ch ☑ Ch ☑ Ch ☐ Ch ☐ Ch ☐ Ch ☐ Ch ☐ Ch ☐
Ch ☐ Ch ☐ Ch1 ☐ Ch1 ☐ Ch1 ☐ Ch1 ☐ Ch1 ☐ Ch1 ☐

SAMPLING FREQUENCY [GS/s]
625.00 ps/sampl
Use External Clock Off / On
Extern Clk Freq: 40.000 MHz

ALL_SAMPICs
POST-TRIGGER ☐ On/Off
x 1/8 Clk Period = 0 ns
"Tour de Piste" DELAY
x 1/8 Clk Period = 0 ns

Recording depth: Shortened / Full
Specified depth: 64 samples
Offset for start of read: 0 samples
Start Read from Trigger Cell + Offset OFF / ON

(a) (b)

Figure 4.2: The settings for the triggering mechanism (a) and the sampling frequency and the delay (b).

4.1.2 Readout with Python

The SAMPIC module saves the acquired data in a text-based DAT file. This file has a specific format to display all the needed information. In the first seven lines, all the acquisition parameters like the sampling rate are shown and the format of the data below is explained. Each of the following three lines belongs to a measurement of a peak. The first of the three lines shows the number and the time of the hit in form of the UnixTime. It is defined as a timer counting in second increments since the first of January 1970. The second line displays different values like the channel number, the value of the baseline, the number of samples and the time of the measurement being saved in nanoseconds. In the third line, the value of the 64 samples is given in volts. These three lines with the new values are then repeated for each hit.

For the analysis of the data, a python program was written. First, the channel number, the baseline and the time in nanoseconds for each hit were read from the second of the three lines. Then the samples of the following line were read and the baseline was subtracted. Since only the absolute value of the amplitude was needed, the samples were additionally inverted. In this place, the different hits can be graphically examined and it can be evaluated if the measurement failed or not.

For further analysis, a function had to be fitted through the data. As a function describing the fluctuations of energy loss by particles in a detector, the Landau distribution is suitable for characterizing the peaks. It is an asymmetric distribution with a gaussian share and spurs to high values for the energy loss [KW16].

An approximation of the distribution was integrated into the program with the Moyal function from the package scipy.stats in python. The corresponding function is

$$f(\bar{x}) = \frac{1}{\sqrt{2\pi}}\exp\left(-\frac{(\bar{x}+\exp(-\bar{x}))}{2}\right) \quad \text{with} \quad \bar{x} = \frac{x-a}{b} \tag{4.1}$$

with the parameters, a and b describing the shifting and scaling of the function [Sci]. As normalization, an additional factor c was multiplied by the function. Even though the Moyal function is only an approximation, it will be referred to as the Landau function in the following. The fitting allowed to calculate position and value of the maxima of the peaks, as well as the position of the point where the peak reaches a certain fraction of the amplitude. These values are needed to measure the full width at half maximum, short FWHM. All the following fits were calculated over orthogonal distance regression with the package scipy.odr from Matplotlib in Python.

For the measured samples the uncertainties of time and amplitude were neglected because all the quantitative analysis of the results was performed on histograms of the different parameters. In such a histogram the distribution of the values is represented since the number of a certain interval and not an exact value is computed anyway. The uncertainty of the values would have no influence on it. The histogram itself has an uncertainty for the x and y values, thus all further calculations with the histograms are performed with uncertainties.

4.2 Plastic Scintillator

4.2.1 Results and Discussion

The first detector used was the plastic scintillator. Figure 4.3 shows the measured samples for one peak. The whole measurement contained 6898 hits. Figure 4.3 also shows the fit of the Landau distribution. As mentioned before, an additional factor c was added to the formula. Therefore, the fitted function was

$$f(x,a,b,c) = \frac{c}{\sqrt{2\pi}} \cdot \exp\left(-\frac{(\frac{x-a}{b} + \exp(-\frac{x-a}{b}))}{2}\right) \tag{4.2}$$

with the fitting parameters $a = 7.13\,\mathrm{ns}$, $b = 1.66\,\mathrm{ns}$, $c = 0.81\,\mathrm{V}$. Using this fit, the maximum of the peak was calculated as $A_{\mathrm{max}} = 0.118\,\mathrm{V}$. The points where the function reaches half of the maximum are also indicated. As already mentioned, these values are all analyzed quantitatively with histograms only, so a calculation of the uncertainty is not necessary at this point. The function and the displayed markers in Figure 4.3 were shifted to the maximum at $x = 0$ in order to be able to examine the course of the different hits by superposition in the next step.

Therefore, the Figure 4.4 shows the shifted Landau distribution together with the same three markers for all the hits. The fitted function again was Equation 4.2.

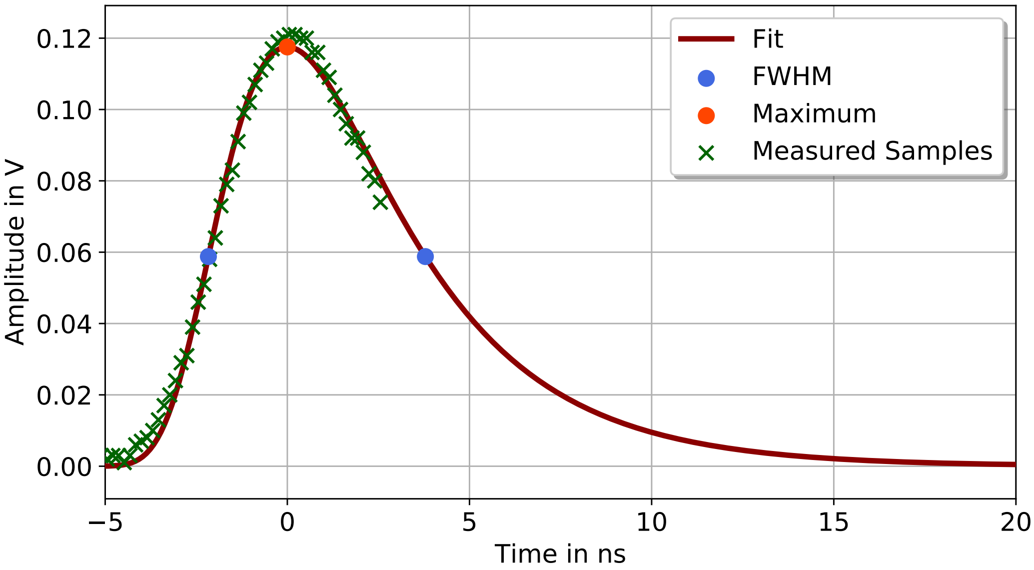

Figure 4.3: The measured samples together with a fit of a Landau distribution, the point where the amplitude reaches its maximum and the two points, where the function reaches half of the maximum. The samples show the amplitude in relation to the time.

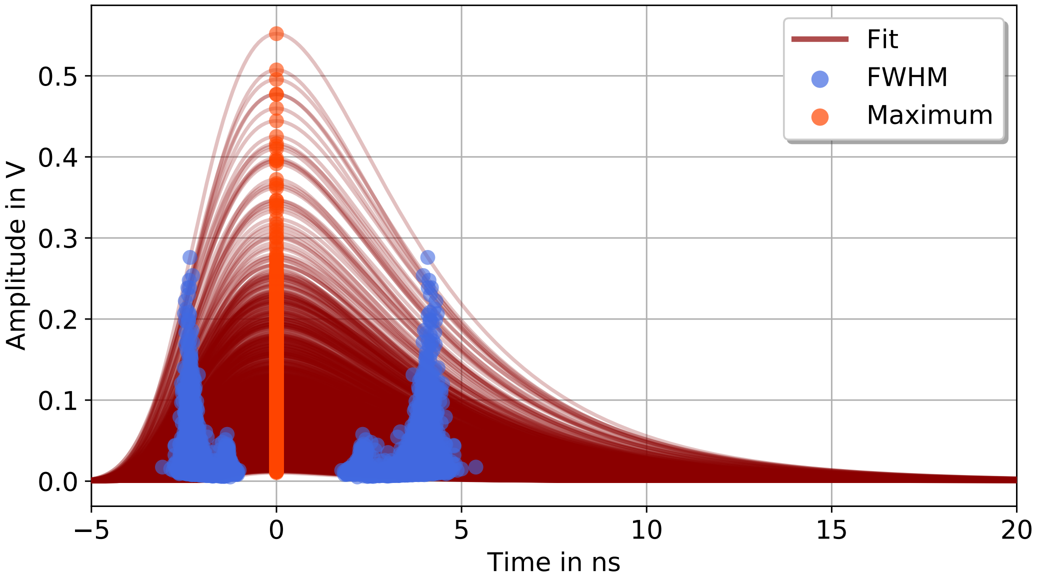

Figure 4.4: The Landau distribution for all the hits together with each point of the maximum and the two points equal to the half value of the maximum corresponding to the FWHM.

In this case, the opacity has been reduced to show areas where different graphs overlap in the form of darkness. While in the area above 0.2 V the course of each individual function is clearly visible, in the area below 0.2 V the number of graphs is too large that it is not possible to distinguish between the individuals. The frequency decreases with increasing amplitude. Normally, an increase in FWHM would be expected with an increase in amplitude. However, in Figure 4.4 it seems, that there are two groups of distributions. One with a slightly smaller width than the other one.

To further examine all the relations, a histogram was created for each of the amplitudes and the FWHM. Figure 4.5 shows the histogram for the frequency of the amplitude for all hits. While about 2000 peaks had a maximum amplitude of approximately 0.02 V, all the amplitudes above 0.4 V were reached only once or twice in the whole measurement. Using a normal y-axis high enough to show the highest bins, almost all bins with a height below 100 would be indistinguishable. Therefore, a logarithmic y-axis with base 10 was chosen. The uncertainty of the different bins is $\sqrt{N}$ with the height N of each bin. This relation for the uncertainty of the frequency will be used for all the shown histograms in the following sections.

To increase the number of bins in the range where more particles occurred, a second histogram was created, in which only a section up to 0.1 V is shown. This histogram is presented in Figure 4.6. A maximum can be seen again around 0.02 V, which is the threshold we set. The reason there are bins below this value is that these hits had

some samples above the threshold, but the fitted distribution calculated a maximum amplitude below 0.02 V. Thus, there could be individual outliers in the measurement, or the reason is the uncertainty of the fit. The course of the different amplitudes seems to be a Landau distribution, which is cut off around the maximum. In an ideal measurement, there would be no noise and the SNR is high enough for every amplitude. In that case, no threshold would be needed and the complete course would be measurable. A real measurement, however, always has noise and the SNR is too low to detect the peaks at a certain point and a threshold is needed.
In Figure 4.6 a Landau distribution with the form of Equation 4.2 and the fitting parameters $a = (1.26 \pm 0.84) \cdot 10^{-2}\,\mathrm{V}$, $b = (6.16 \pm 0.71) \cdot 10^{-3}\,\mathrm{V}$ and $c = 15.9 \pm 9.3$ is shown. The uncertainty for amplitude was $u(A) = 0.17\,\mathrm{V}$, which corresponds to the distance on the x-axis between two points of the histogram. If the intervals of the amplitude are reduced, the distance between two points and thus the uncertainty of the x-axis is reduced. This consideration will be used for all the following histograms. Therefore, just the value of the distance changes.

Because of the missing bins below the threshold, the fit starts at the value of 0.02 V. It is possible, that the bins below 0.02 V would even be higher than the ones above, and therefore a calculation of a fit in that area would not be reasonable for the given data. Due to the low frequency at a certain amplitude, the data becomes more error-prone. Therefore, the fit was just calculated for the data within the area part with a higher

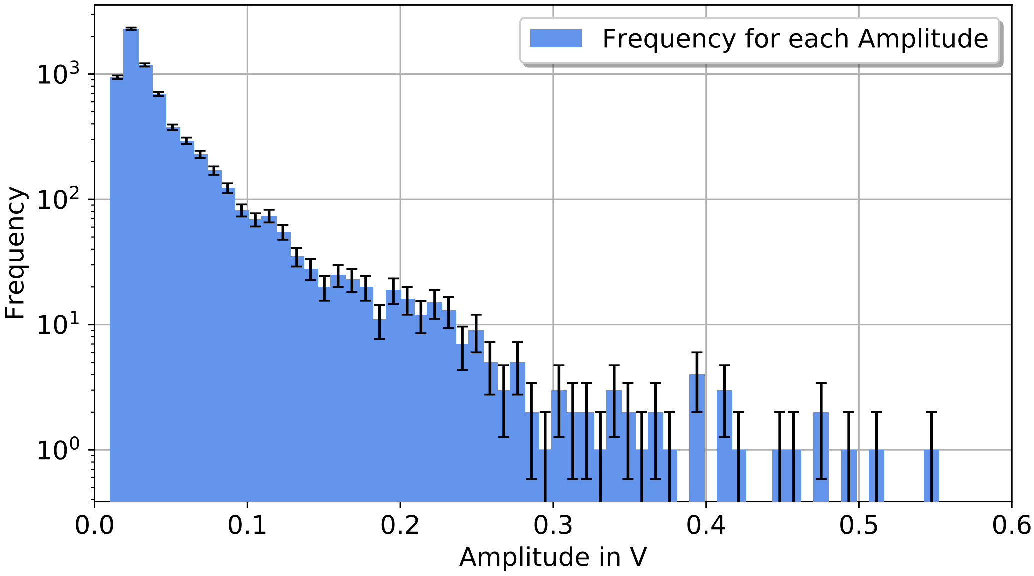

Figure 4.5: A histogram for the amplitude of the measurement with the first detector with the plastic scintillator.

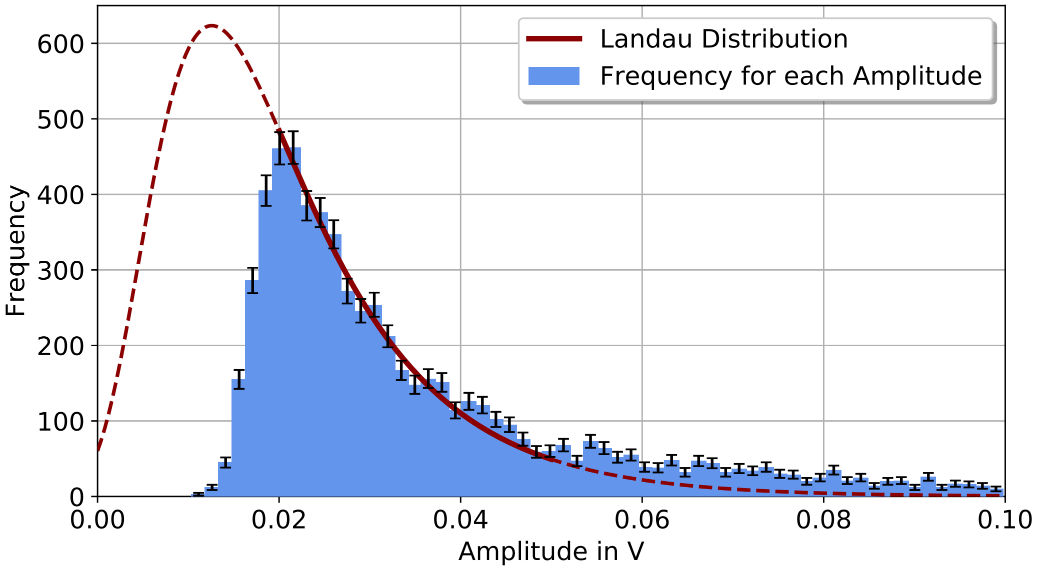

Figure 4.6: A fraction of the histogram in Figure 4.5 compared to a fit of a Landau distribution.

frequency. This range is displayed as a solid line. A dashed line is also drawn for the rest of the histogram to illustrate what the current fit would look like.

The received fit is in the used range within the uncertainties and therefore, it can be assumed that the frequency of the amplitudes can be described with a Landau distribution. This would be consistent with the theoretical considerations of the Landau distribution since it describes exactly such fluctuations of energy. To confirm the theory, the measurement duration could be significantly extended, which should result in more signals in the relevant part and relatively fewer outliers. Most importantly, a more accurate analysis would require a lower threshold and less noise, which was not possible with the given setup.

Figure 4.7 shows a histogram for the frequency of the FWHM in nanoseconds. In this histogram, the observation that two groups of hits with different FWHM occurred can be confirmed. Two stand-alone peaks can be seen and both seem to be Gaussian distributed. To prove the assumption, a fit with the form

$$f(x, \mu, \sigma, a) = \frac{a}{\sqrt{2\pi\sigma^2}} \cdot exp\left(-\frac{(x-\mu)^2}{2\sigma^2}\right) \tag{4.3}$$

was fitted through the data. This function represents a normal distribution with the normalization factor a, the expectation μ and the standard deviation σ. The uncertainty for the x-values in this histogram was $u(\Delta t_{\mathrm{FWHM}}) = 0.11\,\mathrm{ns}$, which lead to the fitting parameters $a = 48.4 \pm 2.4$, $\mu = (3.558 \pm 0.013)\,\mathrm{ns}$ and $\sigma = (0.206 \pm 0.010)\,\mathrm{ns}$

for the smaller left peak and $a = 641 \pm 14$, $\mu = (5.841 \pm 0.013)\,\mathrm{ns}$ and $\sigma = (0.470 \pm 0.011)\,\mathrm{ns}$ for the right and higher peak. The 1σ-range, corresponding to the range of $\mu \pm \sigma$ also shown in Figure 4.7, shows the range in which 68.27% of the hits lay on each of the two gaussian curves. Using the fitted curves, it was confirmed in both cases that the frequency of the FWHM is normally distributed.
The fact that two different peaks were measured could only be explained by an error in the measurement or in the detector itself since the width of the signal should be detector specific. One reason could be, that a few of the particles directly hit the photocathode of the PMT instead of the scintillator. They would have a different energy than the photons from the scintillator and result in a different peak. Because of the significantly fewer particles in the left peak, it must be assumed that this represents the error-prone measurement.

In order to analyse the relation between the amplitude and the FWHM Figure 4.8 shows these values in dependence on each other. The opacity was reduced again to highlight where more points were located. Figure 4.8 visualizes the two peaks for the different sets of FWHM. To investigate a correlation, the mean value was calculated for different amplitudes of the larger peak. The course of the mean values shows an increase in the FWHM when the amplitude increases. Especially in the area where many data points are located, a significant increase can be recognized. As the amplitude increases, fewer data points are present and the mean value begins to fluctuate more and more. Overall, a correlation between amplitude and width can be observed, which is in line with the theoretical expectations.

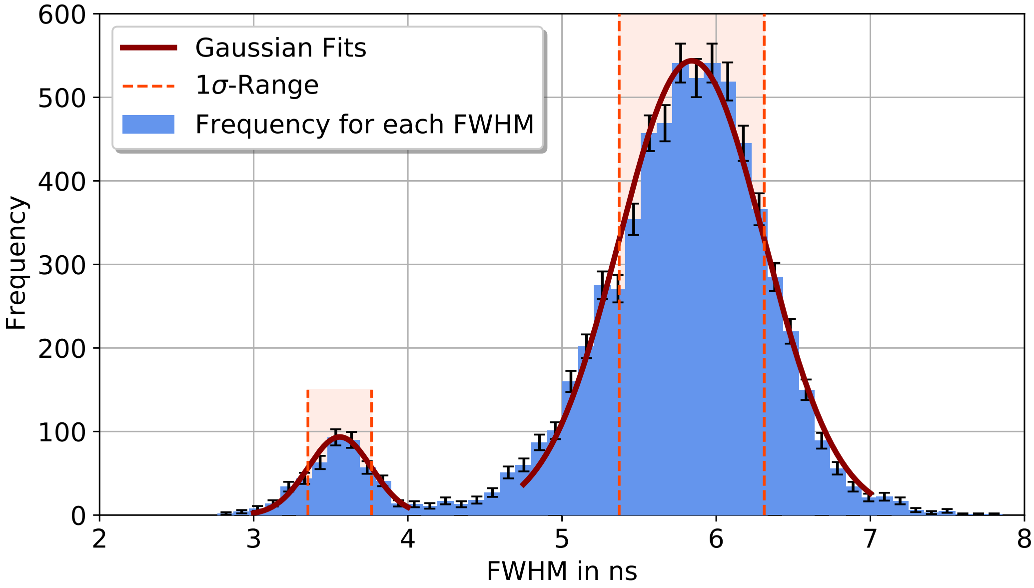

Figure 4.7: A histogram for the FWHM for the measurement using the plastic scintillator. In addition, two gaussian fits and their 1σ-range are indicated.

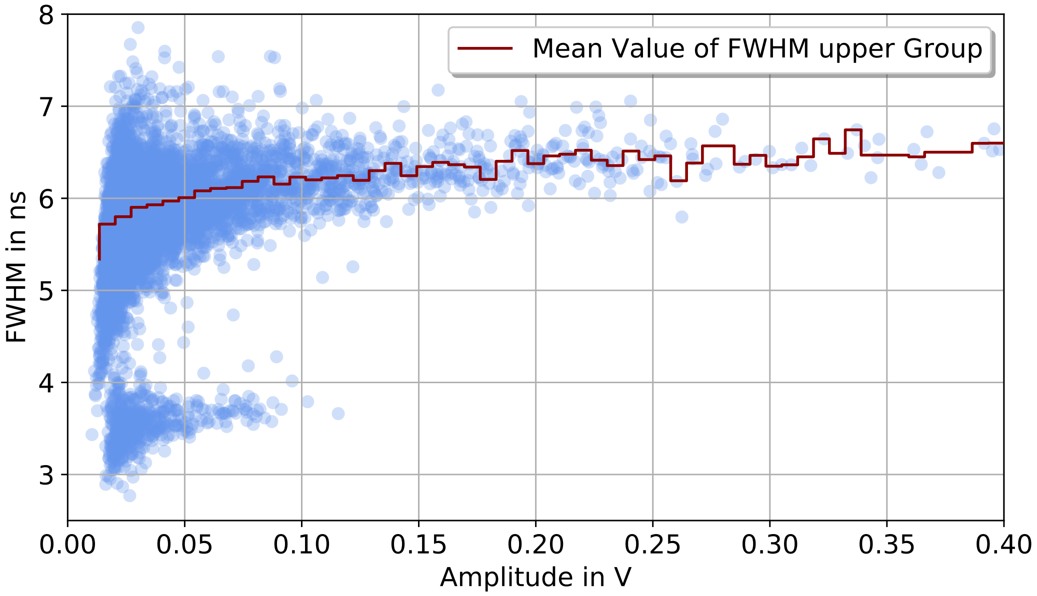

Figure 4.8: The FWHM in relation to the amplitude. To examine correlations, the mean values of the FWHM for different amplitudes are displayed.

4.3 Barium Fluoride Scintillator

4.3.1 Results and Discussion

The analysis of the measurement with the second detector using the BaF_2 scintillator was performed with the same python program as with the plastic scintillator. The performed measurement contained 3351 hits. Figure 4.9 shows the measured samples for one hit together with a fit forming a Landau distribution using Equation 4.2. The fitting parameters were $a = 5.032$, $b = 1.87$, $c = 0.262$. Both, the fit and the samples, were again shifted to have their maximum at $x = 0$. Right at the beginning of the samples at $x = -5$ they are clearly below the fitted curve. In addition, the samples do not flatten out downward on any side but maintain a large slope. This suggests that they represent the top of the Landau distribution and the time window was too short to show enough of the curve needed. Due to this, the fitted distribution is smaller and thinner than it should be. To correct the fit, either an additional baseline had to be added to each measurement to shift the curve upward that the distribution again intersected with all samples, or a measurement with a longer time window had to be done. In order to reduce the error-proneness of the fit, the second solution was chosen. With this, the relevant measurement window was increased too and a more accurate fit could be created.

To increase this length, the sampling rate was reduced to $1.6\,\frac{\mathrm{GS}}{\mathrm{s}}$.

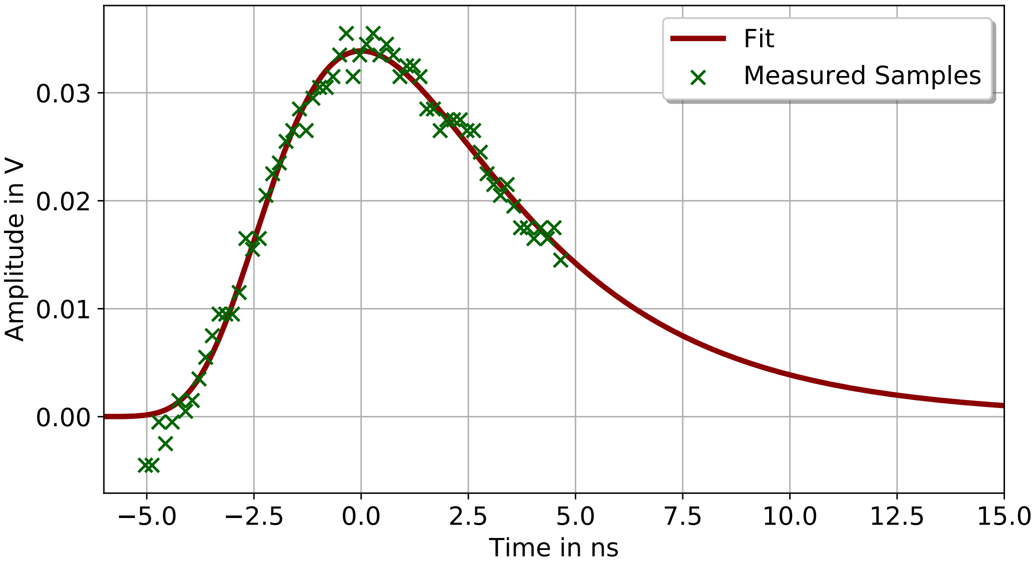

Figure 4.9: The measured samples for one hit with a sampling frequency of $6.4\,\frac{\mathrm{GS}}{\mathrm{s}}$ together with the fit of a Landau distribution. The samples show the amplitude in relation to the time.

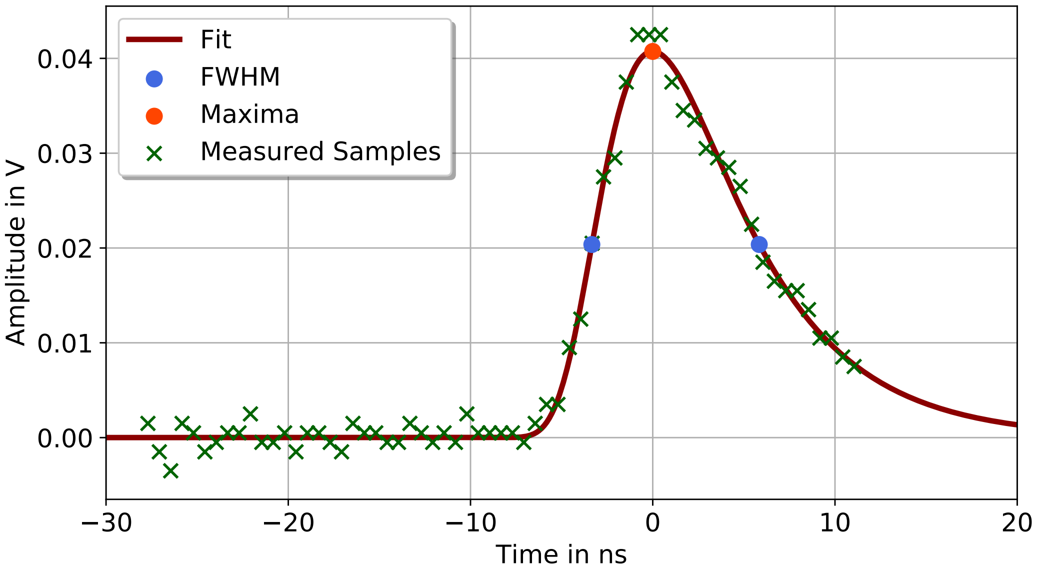

Figure 4.10: The measured samples for one hit with a sampling frequency of 1.6 $\frac{\mathrm{GS}}{\mathrm{s}}$ together with the fit of a Landau distribution. The samples show the amplitude in relation to the time. Also displayed are the maximum and the two points corresponding to the half value of the maximum.

Figure 4.10 shows the shifted samples from one hit along with a fit of the form Equation 4.2. In this case, the samples scatter almost along the entire range where the distribution is above zero and a much more accurate fit is possible. With the calculated fit, the maximum and the points for the FWHM could be determined. The corresponding points are as well shown in Figure 4.10. The fitting parameters were $a = 27.7$, $b = 2.56$, $c = 0.0.431$

The overview for this measurement is in the appendix in Figure A.3.

The distribution of the different amplitudes is shown in the histogram in Figure 4.11, which displays only a section of the total measured distribution, because, similar to subsection 4.2.1, this is sufficient to represent the relevant information. The complete histogram is shown in the appendix in Figure A.4. Again, the bins around the threshold of 0.04 V are the highest. As mentioned in subsection 4.2.1 some of the bins are below the threshold, due to the fitting function being smaller than the highest sample. This can be seen in Figure 4.11 for the described hit. The maximum of the fit is about 0.002 V below the highest sample. Regarding the highest bins being the one right below the threshold it is likely, that even higher or just as high bins would follow for a decrease of the amplitude.

To examine whether the amplitude is Landau distributed or not, Figure 4.11 shows such a fit of the Equation 4.2 with the parameters $a(2.19 \pm 0.51) \cdot 10^{-2}\,\mathrm{V}$, $b =$

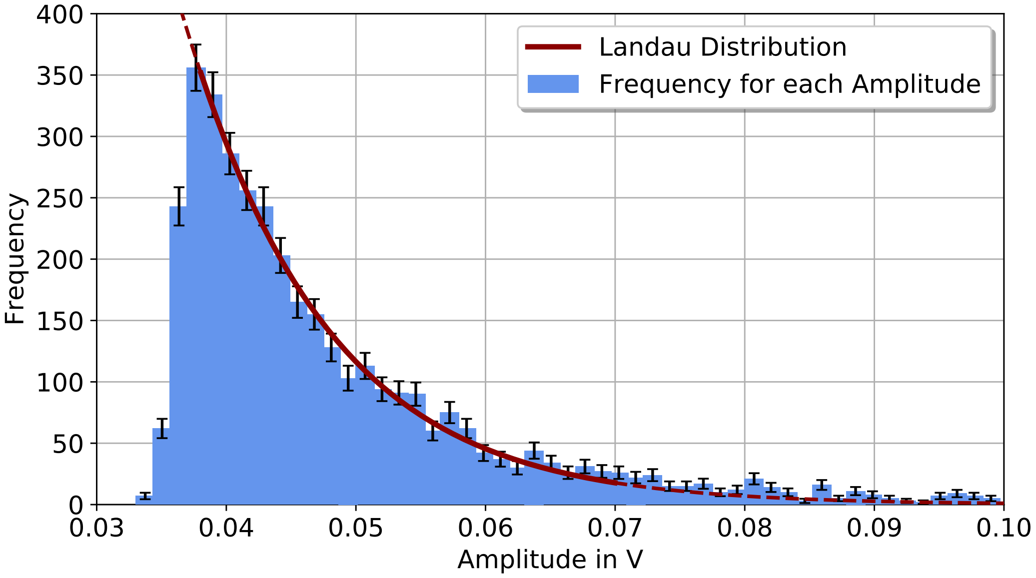

Figure 4.11: A fraction of the calculated histogram for the BaF_2 scintillator together with a fit of a Landau distribution.

$(5.31 \pm 0.75) \cdot 10^{-3}\,\mathrm{V}$ and $c = 21.7 \pm 9.7$. The used uncertainty for the amplitude was $u(A) = 0.0015\,\mathrm{V}$. However, the resulting curve fits the data for the amplitudes above the threshold. For this reason, it can again be assumed that the data is Landau distributed. In measurement with a smaller threshold, the course of the distribution might change a bit, but the coarse distribution should stay the same. Therefore, the same problems as for the plastic scintillator occurred and a more precise measurement would be needed to measure samples below the threshold.

Again, a histogram was created to analyse the FWHM, which is shown in Figure 4.12. It can be seen that the highest bins are at a higher width than in Figure 4.7 and that they only form one peak. Thus, as a first step, the assumption can be confirmed that the two peaks in the measurements of the plastic scintillator were detector specific. In addition, the bins again seem to form a Gaussian curve, which was investigated with a fit of the Equation 4.3. The uncertainty for the width was $u(\Delta t_{\mathrm{FWHM}}) = 0.06\,\mathrm{ns}$, which resulted in the fitting parameters $a = 212.2 \pm 3.3$, $\mu = (8.9538 \pm 0.0071)\,\mathrm{ns}$ and $\sigma = (0.3954 \pm 0.0045)\,\mathrm{ns}$. The calculated course lies within their uncertainty interval for all bins, which is why the assumption that the FWHM is normally distributed can be confirmed. Figure 4.12 shows the 1σ range from $\mu - \sigma$ to $\mu + \sigma$ in which 68.27% of the hits can be found.

With the expectation value $\mu = (8.9538 \pm 0.0071)\,\mathrm{ns}$, the second detector using the $BaF2_2$ scintillator provides wider signals. This is in line with the theoretical assumption of longer rise time for inorganic scintillators.

It was also examined for a possible correlation between the amplitude and the half-width at full maximum. However, since no correlation could be found, the corresponding graph is shown in the appendix in Figure A.5.

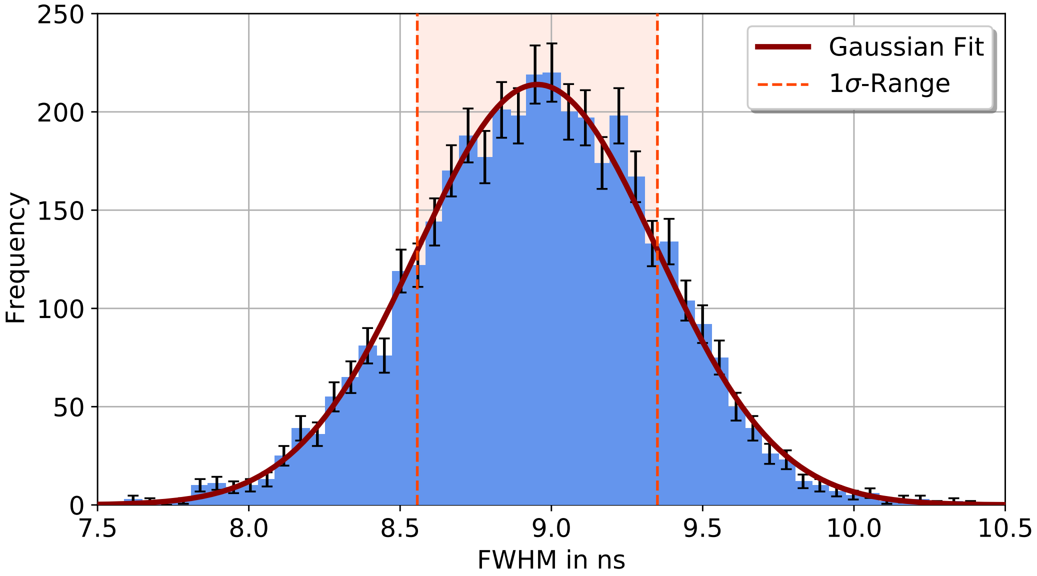

Figure 4.12: A histogram for the FWHM for the measurement using the BaF_2 scintillator. In addition, a Gaussian fit and its 1σ-range are shown

4.4 Coincidence Measurement with both Detectors

4.4.1 Processing the Coincidences with Python

For a better examination of the time resolution of the SAMPIC module, the time difference for the travelling between the two detectors had to be measured. As described in subsection 4.1.1 the settings in the SAMPIC software had to be changed, to just trigger if a particle hits both detectors. But not only the software settings were adjusted, also the python program from subsection 4.1.2 had to be extended. Before fitting the Landau distributions for each hit, the different events had to filter for real coincidences. The saved data also displays the time passing between each measurement. The time had to be read out to calculate the time difference between the two hits of one event. The first filtering was performed to delete all events where the time difference is greater than 20 ns, as this is likely to be a measurement error rather than a true coincidence. Due to filtering with the SAMPIC software, this effect did not occur frequently, but it did exclude one or two events per long time measurement.

Some of the measured hits still were error-prone as shown in Figure 4.13. These hits were filtered out in a second filtering process, where all events with samples below a certain value, like -0.4 V in Figure 4.13, were deleted. The selected filter for an amplitude deleted all events where either the smallest samples of one hit were less than -0.05$\dot{V}$ or the absolute value of the smallest samples was greater than the highest value

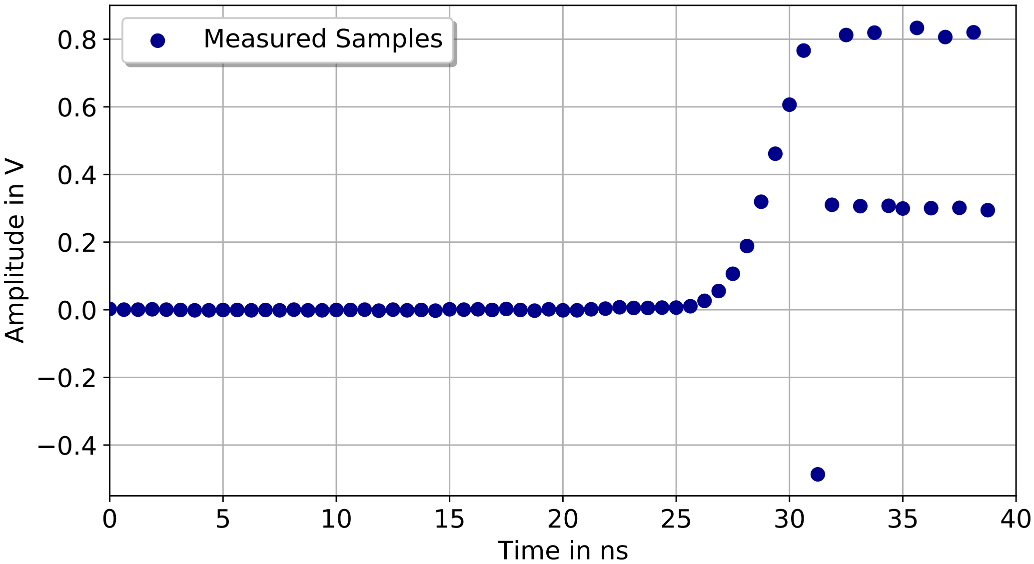

Figure 4.13: The measured samples for one of the hits that had an error and was therefore filtered out. The samples show the amplitude in relation to the time.

of the samples.

In the next step, the Landau distribution with Equation 4.2 was fitted through the hits similar to subsection 4.2.1. In addition, the aforementioned time difference between the measurements of each detector, based on the speed of the SAMPIC chip, was subtracted from the later measurement. Figure 4.14 shows the samples of two hits corresponding to one event together with the fit of Equation 4.2 to visualize the fitting. The fitting parameters were $a = 16.2\,\mathrm{ns}$, $b = 1.89\,\mathrm{ns}$ and $c = 0.173\,\mathrm{V}$ for the fit of detector 1 and $a = 27.1\,\mathrm{ns}$, $b = 2.53\,\mathrm{ns}$ and $c = 0.387\,\mathrm{V}$ for the fit of detector 2. Figure 4.14 additionally shows the points where the distribution reaches $R = 0.5$ of its maximum value. These points will later be used to calculate the time difference between the two hits with the constant fracture as the reference point. The fraction of the maximum was used as the reference point because it is independent of the amplitude of the hit. A simple threshold with a constant value would lead to fluctuations in the time difference, depending on the ratio of the height of the two peaks. In Figure 4.14, it can also be seen that although the maximum from the hit in detector 1 is to the left of the one of detector 2, the points for $R = 0.5$ are the other way around.

The reason for this effect is the different FWHM of the two detectors calculated in the previous chapters. To illustrate this, Figure 4.15 shows the distributions of 5 events, with all peaks shifted by $-x_{\max}$ so that the maximum is at x=0. In addition, their y

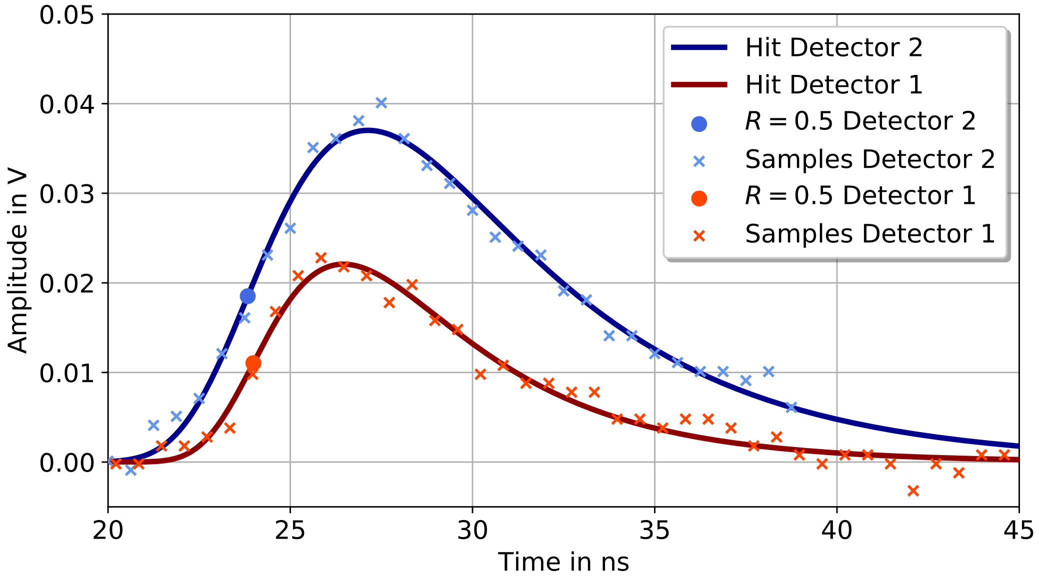

Figure 4.14: The samples and the corresponding Landau distributions for the two hits of one event. The samples show the amplitude in relation to the time. In addition, the figure shows the points where the distribution reaches $R = 0.5$ of the maximum value.

values were normalized by the amplitude height. The first effect shown in Figure 4.15 is, that since the x values were not changed by the normalization, the chosen reference point is always approximately in the same place and is thus actually independent of the amplitude. Due to the relation between the width and the amplitude, all distributions of a detector are approximately exactly on top of each other. The only time difference between the points at $R = 0.5$ for both detectors is based on their FWHM. This difference cannot be justified by the flight time of the particles and results in the reference points in Figure 4.14 being the wrong way around. Therefore, this would lead to a constant deviation of the time differences of the coincidences and had to be corrected. To do so, this difference in the width was subtracted from each of the distributions of detector 1. The result of this calculation for the same 5 events can be seen in Figure 4.16. Due to the shifting all points for $R = 0.5$ for both detectors are approximately on the same spot. If the peaks get shifted back with $+x_{\mathrm{max}}$, the remaining time difference should only be the time difference the particle needed for travelling through both detectors.

The event from Figure 4.14 can be seen in Figure 4.17 including the correction of the FWHM of both detectors. In this case both the maximum and the points of $R = 0.5$ are first for detector 1.

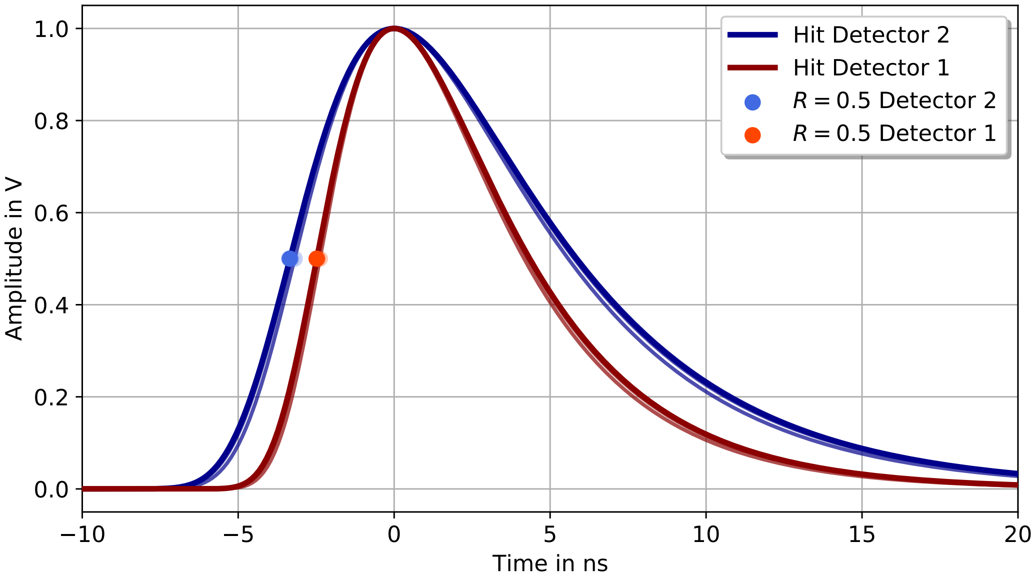

Figure 4.15: The normalized Landau distributions for both detectors for five events shifted to the maximum at $x = 0$.

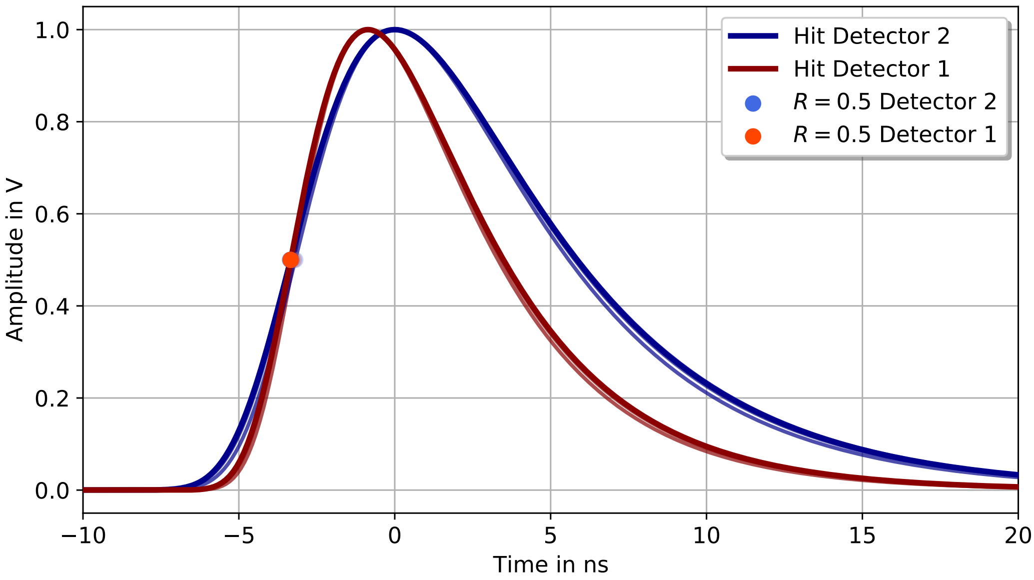

Figure 4.16: The normalized Landau distributions for both detectors for five events with the correction of the different FWHM of the two detectors.

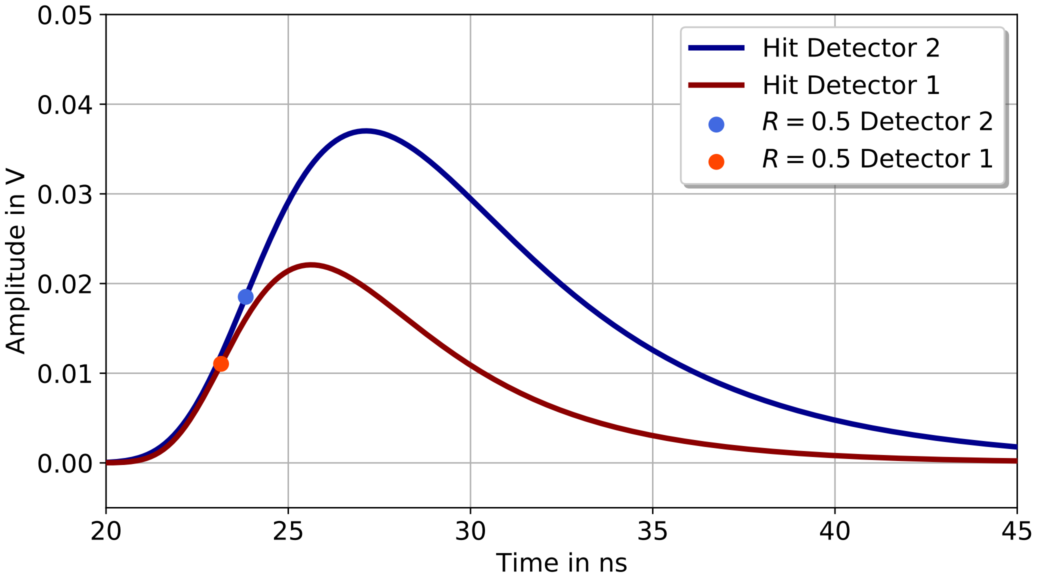

Figure 4.17: The real Landau distributions for both detectors for five events with the correction of the different FWHM of the two detectors.

4.4.2 Results and Discussion

Using the explained python program, the time difference for all the events was calculated and is shown in the histogram in Figure 4.18. The frequency forms a maximum at around $\Delta t \approx 0.7\,\text{ns}$. In the surroundings of this maximum, the distribution seems to form a Gaussian curve. Therefore, Figure 4.18 also shows a fit of the Equation 4.3 and its 1σ-range. The uncertainty of the x-values was $u(\Delta t) = 0.07\,\text{ns}$. Thus, the fitting parameters $\mu_{\Delta t} = (0.6823 \pm 0.0049)\,\text{ns}$, $\sigma_{\Delta t} = (0.2541 \pm 0.0052)\,\text{ns}$ and $a = 163.5 \pm 3.0$ resulted. In Figure 4.18, the solid line indicates which points were used for the fit, while the dashed line is used for visualization purposes only. For the calculation of the parameters, only the part important for the evaluation was used. The foothills, on the other hand, which were very susceptible to measurement errors due to their low frequency, were not taken into account. In the considered interval, the Gaussian distribution describes the measured values and lies in their uncertainty range.

The measured muons traveled approximately at the speed of light $c = 299792458\,\frac{\text{m}}{\text{s}}$ [MS16]. Thus, they would travel about 30 cm in one nanosecond. In the given setup, the two scintillators were placed directly on top of each other. Therefore, if they were identical, the assumed expectation value would be in the magnitude of a few picoseconds and not hundreds. In reality, two different detectors were used. The barium fluoride scintillator not only had a longer signal duration but also consisted

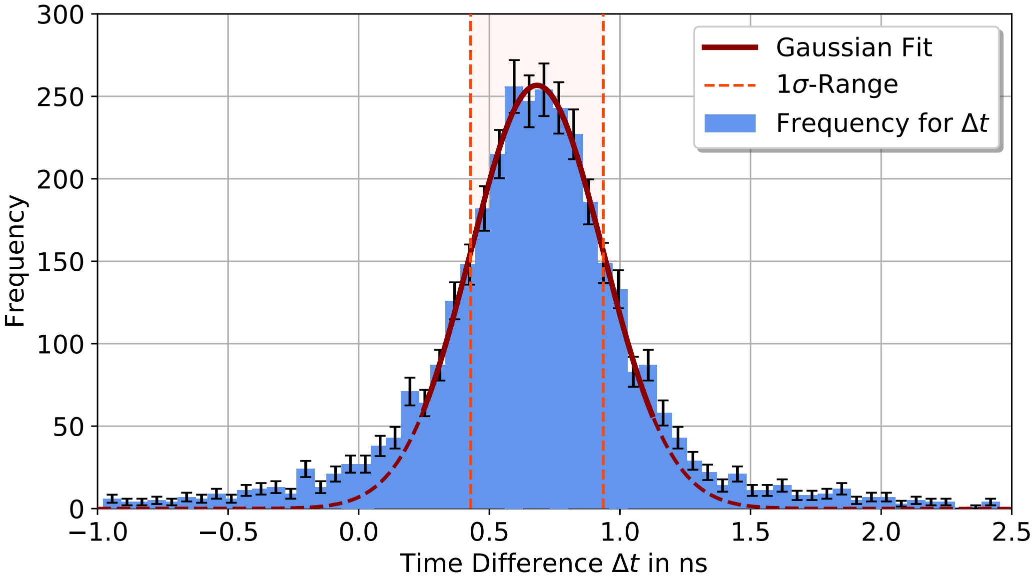

Figure 4.18: The time difference of all the events together with a Gaussian fit and its 1σ-range.

of a significantly larger scintillation crystal. This was just under 20 cm long and also introduced a delay due to the longer path to the photomultiplier. Therefore, the calculated expectation of $\mu_{\Delta t} = (0.6822 \pm 0.0049)\,ns$ is in line with the theoretical expectations for the given setup.

For the time resolution of a plastic scintillator in conjunction with a PMT, a value of about 100 ps is common [KW16]. If a coincidence measurement is performed with two identical detectors, the time resolution for each detector can be calculated with $\sigma/\sqrt{2}$. Even though the detectors used were different, the same calculation was performed to at least classify the results approximately. With the calculated standard deviation the mean resolution for each detector is

$$r = \frac{\sigma}{\sqrt{2}} = (179.7 \pm 3.6)\,\mathrm{ps}. \tag{4.4}$$

The resolution is thus worse than that of a plastic scintillator, which can be explained by the combination with the inorganic BaF_2 scintillator in the setup. It has a poorer time resolution due to its greater signal duration, which decreases the average resolution of both. Due to the combination of detectors in this setup, the resulting resolution meets the expectations. However, a more significant result would be obtained if two identical detectors with plastic scintillators were used. This should improve the resolution and reduce the expected value of the time difference.

To investigate whether the time difference depends on the amplitude, Figure 4.19 shows the ratio between the two values for each hit. The displayed amplitude is the one of the second detectors with the BaF_2 scintillator. The dotted line in Figure 4.19 shows the expectation value $\mu_{\Delta t} = (0.6822 \pm 0.0049)\,\mathrm{ns}$ and the step function displays the mean value of the time difference for a certain range of the amplitude. Theoretically, the time difference should not depend on the amplitude, therefore the step function of an ideal measurement would be a straight line. Especially in the area where many measuring points are located, the mean value is relatively constant in each case and close to the expected value. In the area above 0.15 V far fewer points are displayed and the step function fluctuates more. Due to the low frequency, this part of the distribution is more prone to errors and therefore less meaningful for the analysis. Overall, no trend and thus no dependence between the amplitude and the time difference can be detected. Therefore, no further correction for the amplitude had to be performed.

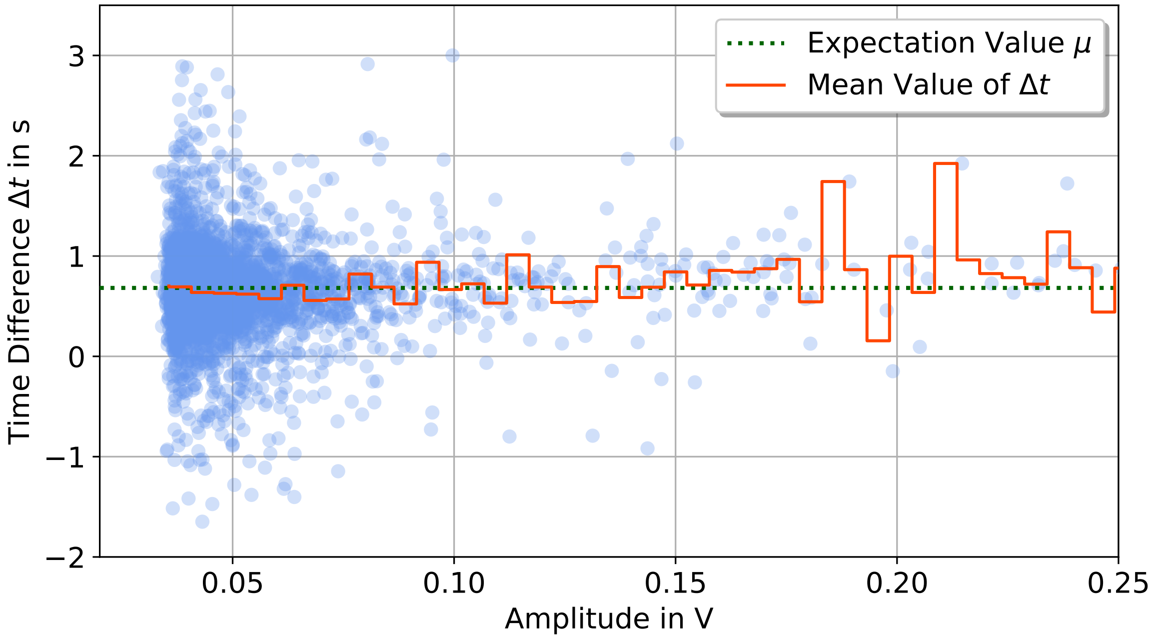

Figure 4.19: The time difference in relation to the amplitude of detector 2 for all the events. In addition, a step function describing the mean value is shown together with the expectation value.

Chapter 5

Conclusion

The first readout of the fast signals was performed with the detector containing a plastic scintillator and a photomultiplier. The samples of each hit could be described with a Landau distribution. For further calculations, the maximum and the full width of the half maximum were taken into account for each hit. This allowed for the creation of a histogram for the maximum amplitude and the FWHM. In the case of the amplitude, the histogram showed a cut-off below the threshold of 0.02 V. Due to some deviation between the fit and the highest samples, some amplitudes below the threshold were calculated. For all the amplitudes above the threshold, a Landau distribution could be fitted through the data and is in the range of the uncertainties. Below the threshold, such a calculation would not be reasonable due to the missing data.

Since the results are consistent with the theoretical expectations that the Landau distribution describes the fluctuations of the energy loss of the particles as they pass through the detector, it does not seem necessary to repeat the measurement. It would only be reasonable to carry out the test again if the noise can be reduced and thus the threshold can be chosen lower. This could increase the range, in which the Landau distribution can be fitted, but should not change the results considerably.

In the histogram of the full width at half maximum two separated peaks could be observed. While the larger peak was expected to occur in this measurement, the smaller one was unexpected and suggests a problem with the setup or measurement. One possible explanation would be, that some of the particles directly hit the photomultiplier instead of the scintillator. Because two peaks were not observed the second detector, an error with the detector is most likely.

With an additional fit, it was shown that the FWHM is Gaussian distributed with an expectation value of $\mu = (5.841 \pm 0.013)\,\mathrm{ns}$ for the larger and presumably error-free peak. For a repeated measurement, a different detector should be used to eliminate

the small and unwanted peak. However, since this would probably only have increased the count rate for the second peak, it was attempted to compensate here by a longer measurement.
In addition, a correlation between the amplitude and the FWHM could be observed.

The second readout was performed with the detector containing an inorganic $\mathrm{BaF_2}$ scintillator. For this detector, the sampling frequency had to be decreased from $6.4\,\frac{\mathrm{GS}}{\mathrm{s}}$ to $1.6\,\frac{\mathrm{GS}}{\mathrm{s}}$ in order to increase the time window of the measurement. Afterwards, the same calculations as with the first detector were performed. In the histogram of the amplitude, the cut-off below the threshold was observed again. The calculated Landau distribution was also within the range of uncertainties for the bins above the threshold. Using the FWHM histogram, the distribution for the second detector was also confirmed to be Gaussian. With an expected value of $\mu = (8.9536 \pm 0.0075)\,\mathrm{ns}$ the FWHM of the second detector was about $3\,\mathrm{ns}$ wider than for the first detector. However, the longer signal duration is in line with theoretical expectations of the inorganic scintillators as $\mathrm{BaF_2}$ having a longer rise and decay time.

To calculate the time resolution of the detectors, the time difference in a coincidence measurement with both detectors was investigated. Therefore, the software had to be adjusted to filter for coincidences and the python program was expanded for calculating the time difference between the detectors. The resulting program filtered out measurements with an error and corrected the time difference due to the computing speed of the SAMPIC and the different values for the FWHM of both detectors. After all corrections were made, the time difference between the points where both courses reached $R = 0.5$ of their maximum amplitude was calculated. The resulting time differences Δt for all events were transferred into a histogram. Apart from the far-reaching foothills, which are considered to be outliers due to their low frequency, the distribution again appeared to be Gaussian. Therefore, a Gaussian curve was fitted through the relevant part of the data. Within that range, the curve was in line with the range of uncertainty of the data. Thus, the expected value for the time difference $\mu_{\Delta t} = (0.6822 \pm 0.0049)\,\mathrm{ns}$ could be calculated. Considering the differences between the two detectors, such as the significantly longer length of the $\mathrm{BaF_2}$ scintillator, the result seems reasonable even though it is higher than the expectation for two identical detectors. The same is true for the the standard deviation $\sigma_{\Delta t} = (0.2541 \pm 0.0052)\,\mathrm{ns}$, which leads to a mean time resolution of $r = (179.7 \pm 3.6)\,\mathrm{ps}$ for each detector. However, the resolution is only an approximation, since the calculation is meant to be for two identical detectors. It was nevertheless performed to be able to classify the result. For plastic scintillators, a resolution of about 100 ps is common, while inorganic scintillators

are much slower and therefore have poorer resolution [KW16]. Therefore, this result seems reasonable and the measurement does not need to be repeated.
Finally, it was investigated whether there was a dependence between the amplitude in one of the detectors and the time difference, which would have to be corrected. This was not the case and the time difference remained approximately constant for the different amplitudes. This is why no correction was needed.

In total, the readout of the signals with the SAMPIC module was successful. The fact, that two different detectors were used led to a worse resolution and a higher time difference for the travel time of the muons. Still, all the results were in line with the theoretical assumptions. Therefore, the SAMPIC software and the python program can be used for new measurements with other detectors.
For the future, measurements with a silicon detector with 32 channels are planned. Such semiconductor detectors are the latest developments for particle detectors. Combined with the high time resolution of the SAMPIC chip, they could exceed current limits.

A Appendix

A.1 Methods, Results and Discussion

A.1.1 Setup

Figure A.1: The detector with the plastic scintillator.

Figure A.2: The detector with the BaF_2 scintillator.

A.1.2 Barium Flouride Scintillator Results

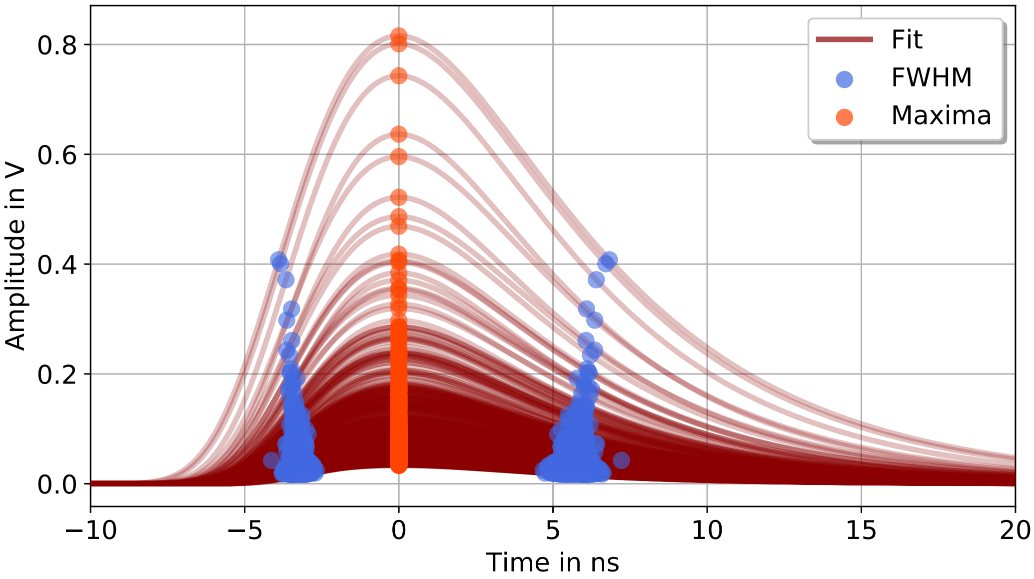

Figure A.3: The Landau distribution for all the hits together with each point of maximum and the two points equal to the half value of the maximum corresponding to the FWHM.

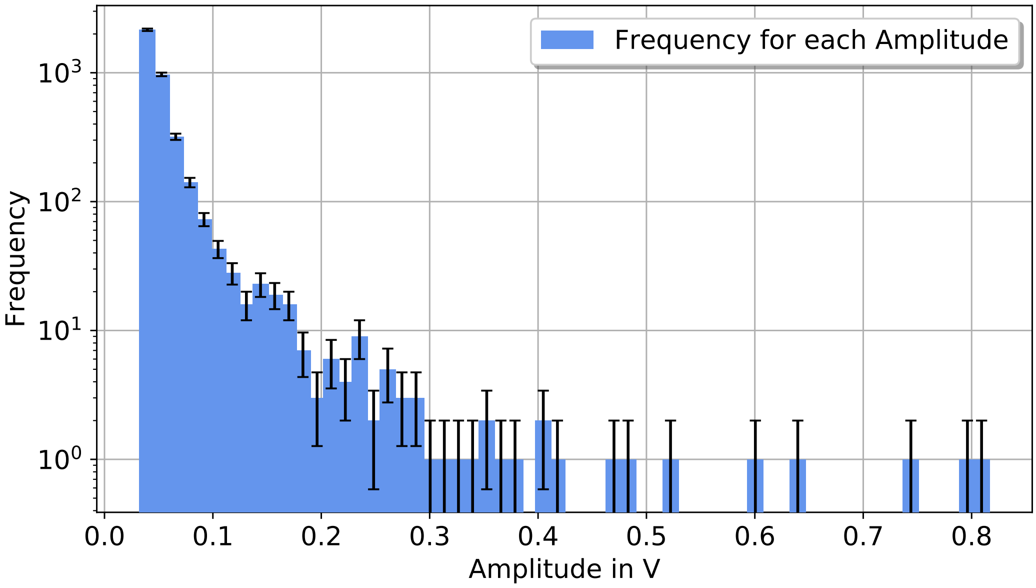

Figure A.4: A histogram for the amplitude of the measurement with the second detector with the BaF_2 scintillator.

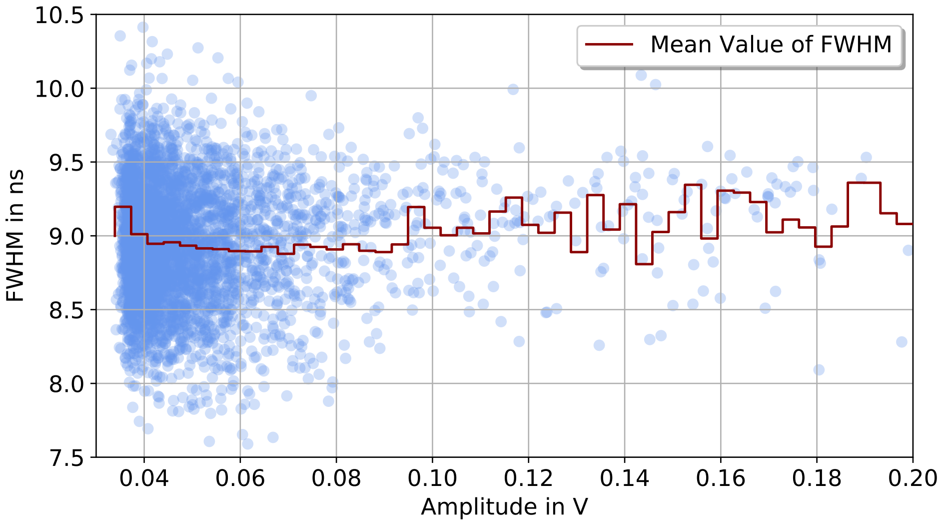

Figure A.5: The FWHM for each hit together with the mean value of the FWHM in relation to the amplitude.

Bibliography

[Bre$^+$16] Dominique Breton et al., *Measurements of timing resolution of ultra-fast silicon detectors with the SAMPIC waveform digitizer.* Nuclear Instruments & Methods in Physics Research Section A-accelerators Spectrometers Detectors and Associated Equipment 835, 51–60. 2016.

[CER22] CERN Collaboration, *The 'Total, elastic and diffractive cross-section measurement' experiment.* URL: `https://home.cern/science/experiments/totem`. 2022.

[Dem17] W. Demtröder, *Experimentalphysik 4: Kern-, Teilchen- und Astrophysik.* Springer-Lehrbuch. Springer Berlin Heidelberg. 2017.

[Gru18] C. Grupen, *Einstieg in die Astroteilchenphysik: Grundlagen, Messungen und Ergebnisse aktueller Forschung.* Springer Berlin Heidelberg. 2018.

[KW16] H. Kolanoski and N. Wermes, *Teilchendetektoren: Grundlagen und Anwendungen.* Springer Berlin Heidelberg. 2016.

[Lec$^+$20] Paul Lecoq et al., *Roadmap toward the 10 ps time-of-flight PET challenge.* Physics in Medicine &amp Biology 65.21, 21RM01. DOI: `10.1088/1361-6560/ab9500`. URL: `https://doi.org/10.1088/1361-6560/ab9500`. 2020.

[Min$^+$17] N. Minafra et al., *Test of Ultra Fast Silicon Detectors for picosecond time measurements with a new multipurpose read-out board.* Nuclear Instruments and Methods in Physics Research Section A: Accelerators, Spectrometers, Detectors and Associated Equipment 867, 88–92. DOI: `https://doi.org/10.1016/j.nima.2017.04.032`. URL: `https://www.sciencedirect.com/science/article/pii/S0168900217304825`. 2017.

[MS16] D. Mende and G. Simon, *Physik: Gleichungen und Tabellen.* Carl Hanser Verlag GmbH & Company KG. 2016.

[Sci] Community SciPy, *scipy.stats.moyal.* URL: `https://docs.scipy.org/doc/scipy/reference/generated/scipy.stats.moyal.html`.

Eidesstattliche Erklärung

Hiermit versichere ich, *Felix Ehring*, dass die vorliegende Arbeit mit dem Titel

„*Readout of fast signals with a multichannel sampling module*“

selbstständig verfasst worden ist, dass keine anderen Quellen und Hilfsmittel als die angegebenen benutzt worden sind und dass die Stellen der Arbeit, die anderen Werken – auch elektronischen Medien – dem Wortlaut oder Sinn nach entnommen wurden, auf jeden Fall unter Angabe der Quelle als Entlehnung kenntlich gemacht worden sind.

Ort, Datum	Vorname, Name

Ich erkläre mich mit einem Abgleich der Arbeit mit anderen Texten zwecks Auffindung von Übereinstimmungen sowie mit einer zu diesem Zweck vorzunehmenden Speicherung der Arbeit in eine Datenbank einverstanden.

Ort, Datum	Vorname, Name